Journal of Computational and Theoretical Nanoscience
Vol. 3, 1–30, 2006

REVIEW

Negative Refractive Index Materials

Victor Veselago,[1] Leonid Braginsky,[2] Valery Shklover,[3] and Christian Hafner[4,*]

[1] *Laboratory of Magnetic Materials, A. M. Prokhorov Institute of General Physics, 38 Vavilov Street, 119991 Moscow, Russia*
[2] *Institute of Semiconductors' Physics, 13 Lavrent'eva Pr., 630090 Novosibirsk, Russia*
[3] *Laboratory of Crystallography, ETH Zürich, CH-8093 Zürich, Switzerland*
[4] *Laboratory for Electromagnetic Fields and Microwave Electronics, ETH Zürich, CH-8092 Zürich, Switzerland*

The main directions of studies of materials with negative index of refraction, also called left-handed or metamaterials, are reviewed. First, the physics of the phenomenon of negative refraction and the history of this scientific branch are outlined. Then recent results of studies of photonic crystals that exhibit negative refraction are discussed. In the third part numerical methods for the simulation of negative index material configurations and of metamaterials that exhibit negative index properties are presented. The advantages and the shortages of existing computer packages are analyzed. Finally, details of the fabrication of different kinds of metamaterials are given. This includes composite metamaterials, photonic crystals, and transmission line metamaterials for different wavelengths namely radio frequencies, microwaves, terahertz, infrared, and visible light. Furthermore, some examples of practical applications of metamaterials are presented.

Keywords: Negative Refractive Index, Metamaterials, Left-Handed Materials, Photonic Crystals, Numerical Methods, Nanotechnology.

CONTENTS

1. INTRODUCTION

Artificial media, i.e., metamaterials may exhibit properties that are much more pronounced than those found in natural materials or they may even exhibit properties that were not observed before in natural media. The most prominent example of not previously observed properties are metamaterials with a negative index of refraction, i.e., Negative Index Metamaterials (NIMs) that are also called Left Handed Materials (LHMs). After first experiments, these metamaterials attracted much interest and were intensively analyzed. Despite of their conceptional simplicity, NIMs provide rich and surprising phenomena and are still not well understood in detail. In the following we present various theoretical aspects together with fabrication issues and focus on the main trends in experimental studies, band-structure calculations, and numerical simulations, that all are necessary for the practical implementation of NIM materials.

2. THEORY OF NEGATIVE INDEX REFRACTION PHENOMENA

In 2000 Smith, Schultz and coworkers[1] demonstrated in their pioneering work that it is possible to fabricate an artificial material with electrodynamic characteristics that can be described by a negative index of refraction n, i.e., a Negative Index Metamaterial (NIM). At that time, the concept of negative index of refraction itself seemed to be new and unusual, although it had been introduced already in 1968[2] by the general consideration of the electrodynamics properties of the materials with simultaneously negative

*Author to whom correspondence should be addressed.

Veselago Victor Georgievich graduated from Moscow University in 1952, and was with P. N. Lebedev Physical Institute, Moscow, from 1952 to 1983. Since 1983 he is head of the laboratory of magnetic materials at the A. M. Prokhorov Institute of General Physics. He received his Ph.D. degree in 1959 for the radiospectropy investigation of molecular spectra and the degree Doctor of Science (solid state physics) in 1974 for the investigation of solid states in high magnetic fields, both at P. N. Lebedev Institute. From 1980 until now he is professor of applied physics at Moscow Institute of Physics and Technology. The main areas of scientific interest of V. G. Veselago are magnetism, solid state physics, and electrodynamics. In his papers, published in 1966–1972, was at the first time considered electrodynamics of material with negative value of refraction index (so called Left-Handed Materials, LHM). V. G. Veselago is a winner of the State Prize for science of USSR (1976), and a winner of the academician V. A. Fock prize (2004). He is also Honoured Scientist of the Russian Federation (2002). He is active as an expert in the Russian Foundation for Fundamental Research and the Russian Foundation for Humanitarian Research. Furthermore, he is vice-chairman of the physics section of the Supreme Attestation Committee of Russia (VAK) and vice-editor of the electronic scientific journal "Investigated in Russia."

Leonid Braginsky was born in Frunze (Kyrgyzstan) in 1956. He received his M.S. degree in theoretical physics from Kyrgyz State University in 1978, and a Ph.D. degree in condensed mater physics from the Institute of Semiconductor Physics (Novosibirsk) in 1999. He is a Senior Researcher at the Institute of Semiconductor Physics and Assistant Professor at the Novosibirsk State University. His research interests include condensed matter theory, electronic and optical properties of low dimensional systems: microstructures, superlattices, nanostructures, quantum dots, and photonic crystals; physical phenomena on an interface, transport and optical phenomena.

Valery Shklover completed both undergraduate and graduate studies in engineering of materials for electronics at Moscow Institute of Fine Chemical Technology in 1971. He earned his Ph.D. (in Russia candidate) in physical chemistry from Nesmeyanov-Institute of Organo-Element Compounds of the Russian Academy of Sciences in 1974 and made his second dissertation (in Russia doctor) in 1981. Under his supervision, six dissertations were prepared. Since 1989 he is working in Switzerland, first at the University of Bern, than at University of Zürich, and since 1991 he is senior scientist at the Laboratory of Crystallography of the Department of Materials of the ETH Zurich. Between 1991 and 1995 V. Shklover was working at the ETH on energy harvesting and storage projects for the Swiss Office of Energy. His main scientific interests are solid-state chemistry, nanostructures, photonics, hybrid organic-inorganic structures, and protection coatings. He is author of more than 120 peer-reviewed publications in Russian and in international journals. He is manager of several industry-oriented projects in the field of nanostructures, protection coatings, sensors. Currently, he owns 5 patents.

Christian Hafner received his diploma, his Ph.D. degree, and venia legendi from the ETH Zurich, in 1975, 1980, and 1987 respectively. Since 1999 he is Professor at the ETH and head of the Computational Optics Group at the Laboratory for Electromagnetic Waves and Microwave Electronics. He is a member of the Electromagnetics Academy. Christian Hafner developed the Generalized Multipole Technique (a semi-analytical method for computational electromagnetics) and various Maxwell solvers, namely the Multiple Multipole Program (MMP)—that was awarded in 1990 by the second prize of the Seymour Cray award for scientific computing—, finite difference solvers in time and frequency domain, mode matching techniques, parameter estimation techniques, and the MaX-1 software package for computational electromagnetics and optics. He also developed various numerical optimizers based on evolutionary strategies, genetic algorithms, genetic programming, and many more. His current research focus is on ultra-dense integrated optics, composite doped metamaterials including materials with low and negative index of refraction, metallo-dielectric photonic crystals, and scanning nearfield optical microscopy.

values of the dielectric permittivity ε and magnetic permeability μ.

The choice of a negative sign for both ε and μ does not cause mathematical contradictions; in particular this does not change the classical expression for n:

$$\eta = \sqrt{\varepsilon\mu} \tag{1}$$

The main question now is how the electrodynamics of the materials with negative ε and μ differ from the electrodynamics of materials with positive ε and μ. There are three possible answers to this "rhetoric" question:

(1) There are no differences, i.e., electrodynamics is invariant with regard to the simultaneous change the signs of ε and μ.
(2) Simultaneously negative values of ε and μ are in principle impossible because this conflicts with some basic principles.
(3) Simultaneously negative values of ε and μ are possible, but the electrodynamics of such materials differs from electrodynamics for the case of positive ε and μ.

It is easy to show that the answer 3 is correct. Let us consider the Maxwell curl equations

$$\begin{aligned} rot\vec{E} &= -\frac{1}{c}\frac{\partial\vec{B}}{\partial t} \\ rot\vec{H} &= \frac{1}{c}\frac{\partial\vec{D}}{\partial t} \end{aligned} \tag{2}$$

For uniform plane waves we obtain

$$\begin{aligned} [k\vec{E}] &= \mu\frac{\omega}{c}\vec{H} \\ [k\vec{H}] &= -\varepsilon\frac{\omega}{c}\vec{E} \end{aligned} \tag{3}$$

One can immediately see from Eq. (2) that the vectors $\vec{E}$, $\vec{H}$, and $\vec{k}$ form a right-handed triple of vectors for positive ε and μ, but a left-handed one for negative ε and μ. For this reason, NIMs are frequently called Left-Handed Materials (LHMs).

Remember that the Pointing vector

$$\vec{S} = \vec{E} \times \vec{H} \tag{4}$$

always forms a right-handed triple of vectors together with the vectors $\vec{E}, \vec{H}$. The direction of the phase velocity $\vec{v}_{ph}$ of the wave coincides with the direction of the wave vector $\vec{k}$, whereas the direction of the group velocity $\vec{v}_{gr}$ complies with the direction of the vector $\vec{S}$. Thus, it is obvious that the phase and the group velocities are antiparallel when ε and μ are simultaneously negative. The inverse statement holds: When the phase and the group velocities of an isotropic medium are antiparallel, the medium is characterized by negative values of ε and μ.

It is important to notice that the antiparallelity of the vectors $\vec{v}_{ph}$ and $\vec{v}_{gr}$ for negative values of ε and μ was already described by Sivukhin[3] and in more detail in the work of Pafomov.[4] More on the history of anti-parallel velocity vectors may be found on the internet.[5] Anti-parallel phase and group velocities immediately affect Snellius' law as illustrated in Figure 1. For positive ε and μ the ray propagates along the way 1–4 through the interface between two media. If one of the media has negative ε and μ, the ray propagates along the way 1–3. This unusual propagation of the ray is a consequence of the opposite direction of the vectors $\vec{v}_{ph}$ and $\vec{v}_{gr}$ and of the continuity of the tangential components of the wave vector on the interface between the two media. Such unusual refraction of waves was discussed probably for the first time by Schuster.[6] Later on, this question was considered more in detail by Mandelstam.[7]

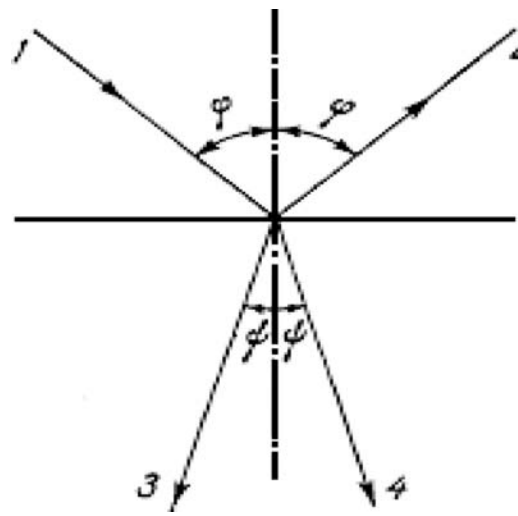

Fig. 1. Snellius law for positive ε and μ (path 1–4) and for negative ε and μ (path 1–3).

If we want to keep the usual notation of Snellius' law

$$\frac{\sin\varphi}{\sin\phi} = n \tag{5}$$

also for negative ε and μ, we must accept that the index of refraction is negative when ε and μ are simultaneously negative or when the vectors of the phase and group velocities are anti-parallel. Exactly in this way, the negative index of refraction was introduced in 1968[2] and even earlier.[8] The appearance of a negative factor of refraction requires rewriting of (1) in more general way

$$n = \pm\sqrt{\varepsilon\mu} \tag{6}$$

Here, the positive sign is used for the usual case, whereas the negative sign is used when ε and μ are both negative.

All the previous considerations imply that the index of refraction n is a scalar, not depending on coordinates and time. It is necessary take into account that n depends on the frequency. Indeed, if the dependency on the frequency (frequency dispersion) would be absent, the energy of the

REVIEW

field $W = \varepsilon E^2 + \mu H^2$ would be negative, when ε and μ are negative. When frequency dispersion exists, the energy W must be written in a different manner:

$$W = \frac{\partial(\omega\varepsilon)}{\partial\omega}E^2 + \frac{\partial(\omega\mu)}{\partial\omega}H^2 \tag{7}$$

This expression is positive for a very broad class of dispersion equations for $\varepsilon(\omega)$ and $\mu(\omega)$. For example, W becomes positive when

$$\begin{aligned}\varepsilon &= 1 - \frac{A_\varepsilon^2}{\omega^2}\\ \mu &= 1 - \frac{A_\mu^2}{\omega^2}\end{aligned} \tag{8}$$

holds. For the special case $A_\varepsilon^2 = A_\mu^2$, (8) easily leads to the interesting correlation

$$\frac{c}{v_{ph}} + \frac{c}{v_{gr}} = 2 \tag{9}$$

For the waves in media with negative index, the wave vector obtains a negative sign. However, in lossy media, the wave vector becomes complex. Its imaginary part is a result of presence of the imaginary parts in the expressions for ε and μ. So, the question arises if the sign of the imaginary part of the wave vector changes, when the sign of its real part changes? To clarify this, we write

$$\varepsilon = \varepsilon' + j\varepsilon'', \quad \mu = \mu' + j\mu'' \tag{10}$$

One can easily see that the wave number k is

$$\begin{aligned}k = k' + jk'' &= \frac{\omega}{c}\sqrt{(\varepsilon' + j\varepsilon'')(\mu' + j\mu'')}\\ &= \frac{\omega}{c}\sqrt{\varepsilon'\mu'}\left[1 + \frac{j}{2}\left(\frac{\varepsilon''}{\varepsilon'} + \frac{\mu''}{\mu'}\right)\right]\end{aligned} \tag{11}$$

when the dissipation is small. From this it follows that the change of the sign of the real part k' does not automatically change the sign of the imaginary part k''. In order to change the sign of the imaginary part of the wave vector, it is necessary to change the sign at the imaginary parts of ε and μ. This corresponds to a transition from a material with positive absorption to a material with the negative absorption as in the case of quantum amplifiers. This transition is not connected to the possible transition from usual materials to the materials with negative refraction.

The fabrication of the composite metamaterials[1,9] that could be characterized by negative values of ε and μ provided a breakthrough for NIM research. The first metamaterials consisted of copper rings and straight wires, disposed in a strict geometric order (see Chapter 5). The straight wires, in essence, are the antennas that interact with the electric field, and rings are the antennas interacting with the magnetic field. The size of these elements and the distances between them are smaller than the wavelength and the whole system may be characterized by a macroscopic model with negative effective values of ε and μ. A direct measurement[9] of the angle of refraction for a prism made of such a metamaterial verified the validity of the Eq. (5) with negative n. The experiment was repeated by several independent groups[10–12] with the same positive result.

The discovery of NIMs poses very important questions: To what extent are all the laws and formulas of electrodynamics, optics, and related technical sciences valid, when n is negative? Can we always simply change the sign $n \to -n$ as, for example, in the case of Snellius' law? In general, the answer to this question is negative. Many laws and equations of electrodynamics and optics correspond to the case nonmagnetic materials with permeability $\mu = 1$. The *nonmagnetic approach* leads to many formulas that drastically change for $\mu \neq 1$. Table I outlines the situation.

As one can see from Table I, there are three groups of physical laws that change when turning from the *nonmagnetic approach* equations to the exact expressions. Snellius' law, Doppler and Cherenkov effects are in the first group. In their formulas, the expression $n = \sqrt{\varepsilon}$ must be replaced by $n = \sqrt{\varepsilon\mu}$. When ε and μ are both negative, a negative sign is also obtained for n.

The laws of reflection and refraction of light and, in particular, Fresnel's formulas, belong to the second group. In these formulas, the value $n = \sqrt{\varepsilon}$ should be changed not to $n = \sqrt{\varepsilon\mu}$ but to $\sqrt{\varepsilon/\mu} = 1/z$, where $z = \sqrt{\mu/\varepsilon}$ is the wave impedance. The wave impedance is a unique feature of each medium, as the speed of light in it. It is important to recognize that it remains positive for negative values of ε and μ. As a consequence, the *nonmagnetic approach* may lead to incorrect equations, for example, when the condition for the absence of reflection of light on a flat border between two media is considered (see Table I).

Table I. Change of some physical laws from $\mu = 1$ to $\mu \neq 1$.

Physical law	Equation for nonmagnetic approach	Correct equation
Snellius, Doppler, Cherenkov $n = \sqrt{\varepsilon} \to n = \sqrt{\varepsilon\mu}$ if $\varepsilon, \mu < 0$, than $n < 0$	$\sin\varphi/\sin\psi = n_{21} = \sqrt{\varepsilon_2/\varepsilon_1}$	$\sin\varphi/\sin\psi = n_{21} = \sqrt{\varepsilon_2\mu_2/\varepsilon_1/\mu_1}$
Fresnel $n = \sqrt{\varepsilon} \to 1/z = \sqrt{\varepsilon/\mu}$	$r_\perp = \frac{n_1\cos\varphi - n_2\cos\psi}{n_1\cos\varphi + n_2\cos\psi}$	$r_\perp = \frac{z_2\cos\varphi - z_1\cos\psi}{z_2\cos\varphi + z_1\cos\psi}$
Reflection coefficient for normal fall of light on the border between two media	$r = (n_1 - n_2)/(n_1 + n_2)$	$r = (z_2 - z_1)/(z_2 + z_1)$
Brewster angle	$tg\varphi = n$	$tg\varphi = \sqrt{\frac{\varepsilon_2}{\varepsilon_1}\frac{\varepsilon_2\mu_1 - \varepsilon_1\mu_2}{\varepsilon_2\mu_2 - \varepsilon_1\mu_1}}$

Finally, there is a third group of equations that strongly depend on n and considerably change when turning from *nonmagnetic approach* to exact formulas, for example, the formula for the Brewster angle. It is important to note that the expression under the square root in the exact formula for the Brewster angle does not change when the signs of ε and μ change simultaneously. Note that the formula for the Brewster angle in Table I corresponds to parallel polarization of the light. For perpendicular polarization, the formula can be obtained from that given in Table I by changing $\varepsilon \to \mu$ and $\mu \to \varepsilon$ in the expression under the square root.

Concerning Table I, we would like to add a consideration of a very important part of geometric optics, known as the Fermat principle. This principle is described in two different versions in the literature:

1. The light spreads from one point of space to another one along the shortest path. Here, term "shortest" implies the minimum of time for passing this way. For example, in the "Physical encyclopedic dictionary," M., Soviet Encyclopedia, 1983 one finds: The ray of light always spreads in space between two points along that way, along which the time of its passing is less than along any other way that connect these points.
2. The light spreads from one point of space to another one on a path that corresponds to the minimum length of the optical way (minimum optical length). For example, in the British encyclopedia (http://www.britannica.com/search?query=Fermat%60s%20principle&ct=&fuzzy=N) one finds: Light traveling between two points seeks a path such that the number of waves (the optical length between the points) is equal, in the first approximation, to that in neighboring paths.

Note that the term "minimum" (of way or time) should be replaced in some cases by the term "maximum" and sometimes by "extremum." To clarify this, we now pay attention to the two formulations of Fermat's principle. Obviously, that both formulations are correct when light passes through usual, Right-Handed Material (RHM), but they both are not correct, when the light partly passes through a RHM and partly through a LHM.

This is confirmed by Figure 2 that illustrates the possible ways of a ray crossing a flat surface between two media with the indices of refraction n_1 and n_2 respectively. If n_1 and n_2 are both positive, the ray travels along AO_1B, and angles φ and ϕ satisfy Snellius' law $n_1 \sin\varphi = n_2 \sin\phi$. The optical length of this way L is

$$L = n_1(AO_1) + n_2(O_1B) \tag{12}$$

It is not difficult to show that Snellius' law (5) is valid if and only if the variation of the optical length δL is zero:

$$\delta L = \delta\{n_1(AO_1) + n_2(O_1B)\} = 0 \tag{13}$$

Here, the length L for AO_1B is minimum and positive.

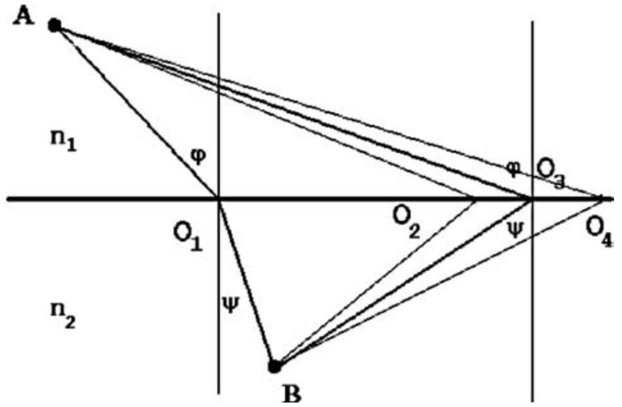

Fig. 2. Light propagation from point A to point B through a flat interface between two media with refraction indices n_1 and n_2. Case $n = n_1/n_2 > 0$: The light travels along AO_1B. Case $n = n_1/n_2$: Light travels along AO_3B. The ways AO_2B and AO_4B are virtual ways illustrating Fermat's principle.

In the case, when both n_1 and n_2 are negative, the propagation of the ray will be the same as in the previous case, but with one important difference. In the first case, the wave vector in both media is directed along the rays, i.e., from A to B, but in the second case the wave vector is directed against the direction of the rays, i.e., from B to A. Thus, the optical length L turns out to be negative, and for AO_1B it will be a maximum. Note that both cases correspond to $n = n_2/n_1 > 0$.

The situation greatly changes if $n = n_2/n_1$ is negative. A RHM is then on one side and a LHM on the other side. Light will then propagate along the way AO_3B and one obtains

$$\delta L = \delta\{n_1(AO_3) + n_2(O_3B)\} = 0 \tag{14}$$

This expression changes when a negative n is introduced for the LHM. Therefore, the condition "extremum of the optical length" is valid. However, in this case it is impossible to confirm *a priori* that the real way of light corresponds exactly to the maximum or exactly to the minimum of the optical way. The type of the extremum depends on the geometry and on the values n_1 and n_2. Furthermore, the real way from A to B is not the shortest in terms of spreading time, i.e., the formulation of Fermat's principle by the time of spreading is not correct in general. The correct formulation is based on the extremum of the optical length: "The real way of spreading light corresponds to the local extremum of the optical length." Using the term "local" takes into account that there can be several possible optical ways that fulfill the equations (2) and (3).

The optical length L between the points A and B in most common case—when the index of refraction is changed from point to point—is equal to the integral

$$L = \int_A^B n\,dl \tag{15}$$

Since the value n in Eq. (4) can be negative, it is clear that the optical length L (this value is really an eiconal)

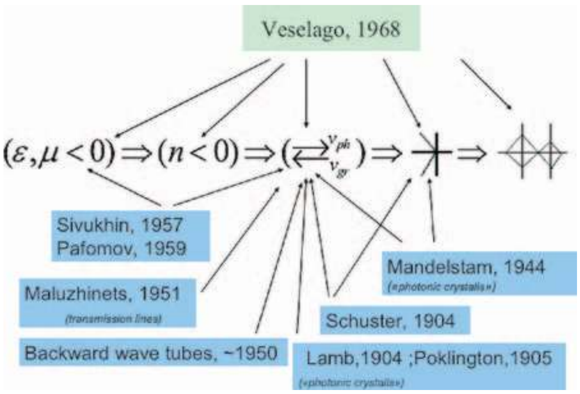

Fig. 3. Early studies of the negative refraction phenomenon.

can have any sign and any value. So, this length will be negative if the light passes through LHM only. In special cases, the optical length is equal to zero. Exactly such a zero optical length between an object and its image is observed for a flat LHM lens, i.e., the NIM slab that is considered in more detail in Chapter 4.

The concept of the optical length is connected with the total phase wind of the wave that depends on the index of refraction n, which defines the phase velocity of light, rather then the group velocity. As it is well known, group and phase velocities are different in dispersive media.

The antiparallel orientation of the vectors of the phase and group velocities is an essential condition for negative refraction. Such antiparallel orientation corresponds to so-called "backward waves," or negative group velocity. In our opinion, the term "negative phase velocity" would be more appropriate, bearing in mind that the group velocity, directed from the source to the receiver, is always positive.

The logical scheme linking the notions "simultaneously negative values of ε and μ," "negative factor of refraction," "backward waves" and "negative refraction" is outlined in Figure 3. The authors and the dates of the first publications of the scheme elements are also specified. The scheme in Figure 2 presupposes that negative refraction appears when we have backward waves in an isotropic material that is characterized by negative values of ε, μ, and n. However, the use of materials with negative values of ε, μ, and n is not the only way to obtain backward waves and hereby negative refraction. Moreover, backward waves exist in many systems that cannot be described by negative permeability and negative index of refraction. The well known backward waves in vacuum electronic devices are a typical example. In such devices the phenomena of negative refraction can be not obtained. A long time ago, backward waves in transmission lines were also studied.[1] Negative refraction can not be obtained in these uniaxial structures, but the main phenomena that are typical for LHMs are present in recently proposed 2D and 3D transmission line structures obtained from LC circuits.[1,2]

Figure 3 illustrates the history of backward waves and of negative refraction. The relation between backward waves and negative refraction was shown for the first time by Shuster[6] in 1904, and then in more detail by Mandelstam[7] in 1944. Both Shuster and Mandelstam referred to earlier work by Lamb.[16] Mandelstam and Lamb considered linear mechanical structures—equivalent to photonic crystals—rather then two- or three-dimensional media with negative ε, μ, and n. Also Poklington[17] studied a linear mechanical model that provided backward waves.

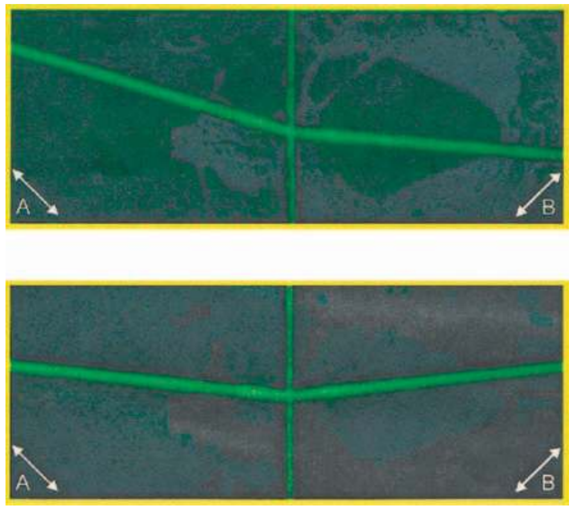

Fig. 4. Light propagation in a YVO_4 bicrystal. Normal (positive) and abnormal (negative) refraction. Reprinted with permission from [19], Y. Zhang et al., *Phys. Rev. Lett.* 91, 157404 **(2003)**. © 2003.

Concerning the realization of negative refraction, it is important to mention a very widespread and well-explored class of materials that provide negative refraction: Anisotropic crystals. It is well known that the directions of refracted rays, phases, and group velocities do not coincide both in anisotropic crystals and in materials with negative refraction, as shown in Figure 4. The observed ray propagation in the crystal corresponds to the ray propagation in the case of negative refraction, but the material properties cannot be described by a scalar refraction index n because the permittivity ε—that defines n- is a tensor. Thus, negative refraction may occur without a negative index of refraction! Following Zhen Ye,[19] this case may be called "quasi-negative refraction."

The term "backward wave" should also be handled with care. We use the term "backward wave" when the vectors $\vec{S}$ and $\vec{k}$ (and, accordingly, the phase and group velocity) are antiparallel, as it is shown on Figure 5. However, the following broader definition of direct and backward waves is also used:[20] When the scalar product of the phase and group velocities is positive

$$\vec{v}_{ph} \cdot \vec{v}_{gr} > 0 \tag{16}$$

the corresponding wave is defined as forward wave and when

$$\vec{v}_{ph} \cdot \vec{v}_{gr} < 0 \tag{17}$$

hold one has a backward wave. It is obvious that one has an intermediate case when the vectors $\vec{v}_{ph}$ and $\vec{v}_{gr}$ are

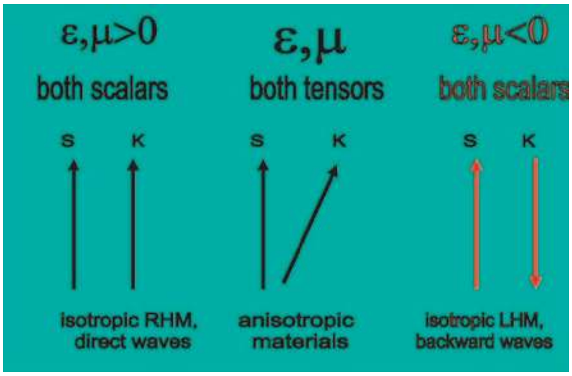

Fig. 5. Schematic of direct and backward waves.

oblique rather than parallel (RHM) or anti-parallel (LHM), as illustrated in Figure 5.

The diagram in Figure 6 shows all possible combinations of signs of ε and μ. The first quadrant corresponds to the materials with positive refraction, third quadrant corresponds to the materials with negative refraction, but the second and fourth quadrant corresponds to materials that do not permit electromagnetic wave propagation, i.e., that will simply electromagnetic waves without energy dissipation. A typical example is plasma in the ionosphere with $\mu = 1$, but negative ε in accordance with Eq. (8).

Now, the question is: in what kind of materials can we observe negative refraction? This question was answered by Smith, Schultz, and co-authors[1]—based on some theoretical work of Pendry[21,22]—who fabricated a metamaterial, i.e., an artificial structure consisting of straight metallic wires—responsible for the negative permittivity—and metallic split rings resonators—responsible for the negative permeability. Furthermore, it was experimentally demonstrated that one may obtain artificial dielectrics and magnetics based on an ensemble of metallic parts, forming some sort of ideal gas of conducting particles. This idea was probably published first by Gorkov and Eliashberg.[23] However, the studies of Gorkov and Eliashberg, and recent work of Pendry, Smith, and Schultz do not imply that materials with negative refraction can only be produced as artificial dielectrics and magnetics. One of us (VV) spent significant efforts for obtaining materials with negative refraction based on magnetic $CdCr_2Se_4$ semiconductors.

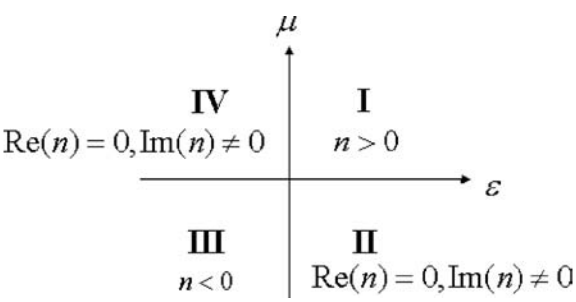

Fig. 6. All possible combinations of ε and μ.

Up to now, these efforts failed because of technological difficulties.

The discovery of NIMs with their surprising electrodynamic properties attracted much interest and also provoked statements of questionable value. For example, Valanju et al.[25] say that negative refraction exists only for the phase velocity, whereas the usual law of refraction holds for the group velocity. The authors do not realize that the difference in the directions of phase and group velocities is a typical for the optics of anisotropic media that can not be characterized by a scalar refraction index. This mistake originates from the muddle of the direction of the group velocity and the direction of the normal to the surface of constant amplitudes of modulated waves.[26]

The problem of overcoming the diffraction limit or, in other words, the problem of amplification of so-called evanescent modes is also closely related to NIMs since Pendry[27] stated that one may have waves in such a medium with

$$k_z = \sqrt{\frac{\omega^2}{c^2} - k_x^2} \tag{18}$$

purely imaginary, where z is the direction of the propagation. This holds for sufficiently large k_x only. In material with positive n the amplitude of such waves (the evanescent modes) exponentially decay along the z axis, and this finally explains why the resolution of optical systems is limited and cannot be much smaller than the wavelength. Pendry[27] (and many others after him) pointed out that the amplitude of evanescent waves with imaginary k_z increases in NIMs or in LHMs. He considered the simple device, consisting on a NIM slab as shown in Figure 8 and confirmed that the classical diffraction limit is not valid for such a "super lens." He and many others did not consider that overcoming the diffraction limit automatically means breaking the uncertainty principle. For our case the uncertainty equation can be written as follows

$$k_x d \geq 2\pi \tag{19}$$

Here k_x is the component of the wave vector orthogonal to z axis (direction of the propagation) and d is the transverse size of a focused spot of light. The k_x value can not be larger than the wave vector k_0 in the free space:

$$k_x < k_0 = \frac{\omega}{c} = \frac{2\pi}{\lambda} \tag{20}$$

From Eqs. (19) and (20) immediately follows:

$$d > \lambda \tag{21}$$

Admitting the possibility of breaking the diffraction limit is equivalent to discarding Eq. (21), i.e., not accepting the uncertainty principle. This would be an extremely far reaching statement of much higher importance than all other statements about the characteristics of materials with negative refraction index. This statement originates from

REVIEW

REVIEW

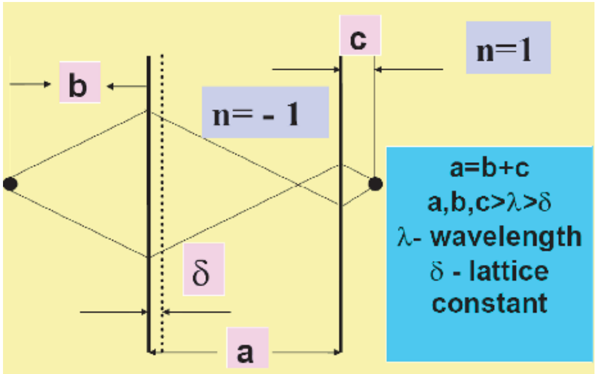

Fig. 7. Flat lens produced by a material with refraction index $n = -1$ (NIM slab).

a not very precise use of some terms, namely "lens" and "resolution." Usually, "optical lens" characterizes an optical instrument that is essentially explained by the laws of geometric optics. Pendry's "perfect lens," i.e., a flat NIM slab as is shown in Figure 7 can be considered as an "optical lens," only when

$$a > \lambda > \delta \tag{22}$$

holds, where a is the slab width, λ the wavelength, and δ the period of the internal metamaterial structure. Besides, for a NIM slab with $n = -1$ in free space ($n = 1$) one has

$$a = b + c \tag{23}$$

The NIM slab may be considered as an "optical lens" only when (22) holds and this was originally Veselago's[2] assumption although this was not explicitly indicated. However, Pendry[27] and others considered cases where (22) does not hold. Such a system is rather some matching device than an "optical lens." For matching devices, it is well known that the flow of energy can be focused on a spot that is undoubtedly smaller than the wavelength.

To clarify the situation, let us consider electromagnetic waves in an usual metallic waveguide of rectangular cross section. It is well known, that electromagnetic wave propagates when

$$\lambda < 2a \tag{24}$$

where a is the longer side the waveguide. When this condition is satisfied, the output of such a waveguide can be considered as some rectangle image formed by the cross-section of the waveguide. The size of this rectangle is of order a. For measuring the fields in the waveguide one must use detectors that must are smaller than the size of the waveguide. If such a detector is located near the output end of the waveguide, it will register only a small part of radiation. If we want to enlarge the power imping-ing on the detector, we can use matching devices—usually screw and slots—in the vicinity of the detector as outlined in Figure 8. The increase of the detected power could be considered as focusing radiation to the spot where the

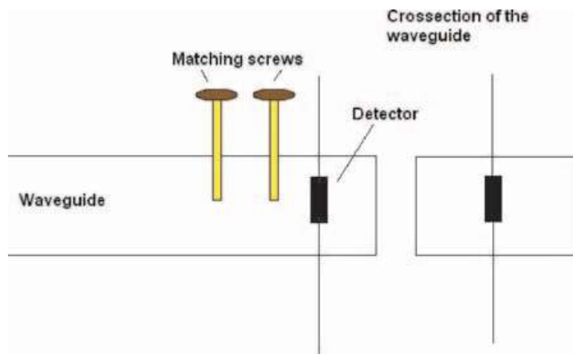

Fig. 8. Simple matching device for a detector in a waveguide.

detector is and this spot may easily be much smaller than the wavelength. However, such a set of screws would never be called "lens."

3. NEGATIVE REFRACTION IN PHOTONIC CRYSTALS

The lattice constants of common materials are 0.2–1 nm, i.e., much below the wavelength of visible light (a few 100 nm). This is the reason why the response of such materials on the electrical and magnetic fields of light wave can be described by the macroscopic parameters ε and μ. The sizes of "atoms," i.e., wires or split ring resonators, in the NIMs mentioned above are comparable with the distances between them. A similar relation between the size of "atoms" and the lattice constant holds for so-called Photonic Crystals (PhCs), proposed by Jablonovich[29] in 1987. PhCs are the metamaterials composed of dielectric or metallic parts ("atoms") arranged on 2D or 3D periodical lattices.

Light propagation in the PhCs cannot be considered as an average effect of the "atoms" as in common crystals. In contrary, light propagation in PhCs is the result of Bragg diffraction at each "atom." Hence the periodical structure of the PhCs is very important. The macroscopic constants ε and μ cannot describe the light propagation in PhC and the light refraction at the PhC boundary. More precisely, light waves in PhCs should be considered as the Bloch waves, but in the so-called envelope function approximation they may be considered as plane waves.[30–34] Furthermore, the commonly used boundary conditions (continuality of the tangential components of the electric and magnetic fields) must be generalized.[35,36] As a result, Snellius' law for PhC obtains the form

$$\frac{\sin\varphi}{\sin\phi} = n(\varphi) \tag{25}$$

Note that n is now a function of the incidence angle.

Negative refraction in PhCs is due to the peculiarities of their photonic band spectra. At first sight, the effect arises because of the negative slope of the upper band, and the existence of the photonic band gap seems to be

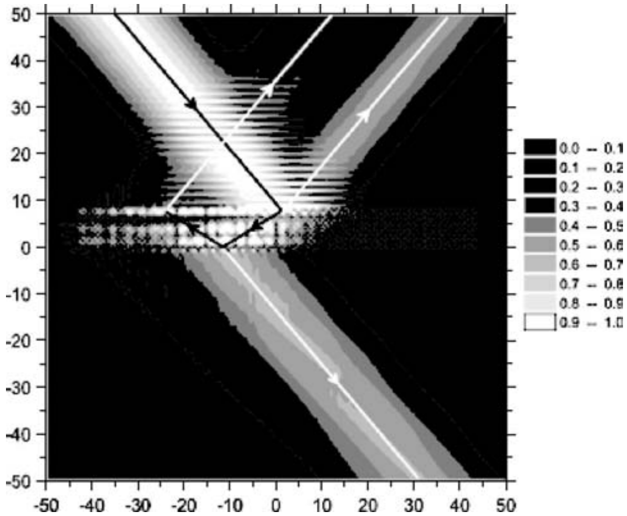

Fig. 9. Modulus of the light field of a polarized Gaussian beam incident on a crystal consisting of 69×7 rods in vacuum. The stationary waves above the crystal are due to interference of incident and reflected waves. Straight lines show the maximum incident (black), transmitted, and reflected (white) fields. Reprinted with permission from [37], B. Gralak et al., *J. Opt. Soc. Am. A* 17, 1012 (**2000**). © 2000.

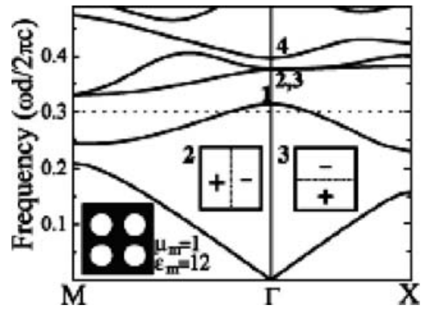

Fig. 10. Band structure of the 2D photonic crystal shown in the left bottom inset. Points M and X corresponds to the directions [11] and [10], respectively. Dashed line indicates the working frequency. Central insets show parity of the electric field in a unit cell for bands 2, 3 at $k = 0$. Reprinted with permission from [40], A. L. Efros and A. L. Pokrovsky, *Sol. St. Comm.* 129, 643 (**2004**). © 2004. A. L. Pokrovsky and A. L. Efros, *Sol. St. Comm.* 124, 283 (**2002**). © 2002.

not important. However, this is not correct. Indeed, the negative slope of the upper photonic band is the result of the reduction to the first Brillouin band. The phase of the Bloch wave $\vec{E}_{n\vec{k}}(\vec{r})e^{i\vec{k}\vec{r}}$ consists not only of the exponential factor $e^{i\vec{k}\vec{r}}$, but also of the phase of the Bloch amplitude $\vec{E}_{n\vec{k}}(\vec{r})$. In particular, in the model of an empty lattice the total phase factor is $e^{i(k-2\pi/d\,\mathrm{sgn}k)r}$, i.e., the sign of the wave vector coincides with the slope of the band. Negative refraction can be expected only in the vicinity of the photonic band gap, where the arguments above fail.

Negative refraction in systems with photonic band gaps was explored by Gralak and co-workers[37] in a numerical study of light propagation through a two-dimensional PhC slab. This simulation provided an explicitly perceptible negative refraction (Fig. 9). Light refraction in PhCs was further numerically investigated for 2D[38] and for the 3D PhCs.[39] More details on numerical simulations are given in the following section. The interpretation of the mechanism becomes more clear when the photonic band structure (Fig. 10) is analyzed. The second photonic band (band 1 in the Fig. 10) behaves like a hole band in semiconductors. The group velocity of the photons in this band is negative, i.e., $\partial\omega/\partial k < 0$. Therefore, negative refraction has to be expected for light impinging on the PhC from a homogeneous material. Apparently, the effect should not be a simple consequence of the band folding. In any case it should not take place in an empty-lattice PhC.[34] Negative refraction in the PhC is a result of the band gap and has to be observed in the vicinity of the band gap, at the Γ point.

The theory of the negative refraction in PhC[40] is outlined in the following. A simple 2D photonic crystal consisting of cylindrical holes arranged on a square lattice in a homogeneous medium with $\varepsilon_m = 12$, and $\mu_m = 1$ (see left inset in Fig. 10). Cartesian coordinates with z-axis along the cylinder axis are used. The electromagnetic energy density of s-waves (the electric field **E** is polarized in z direction) is:[42]

$$W = \frac{1}{16\pi\mu_\perp\omega}\frac{\partial(\omega^2 n^2)}{\partial\omega}|\vec{E}|^2 \tag{26}$$

where $\mu_\perp = \mu_{xx} = \mu_{yy}$ and $n^2 = \varepsilon_{zz}\mu_\perp$. When $W > 0$, one obtains $\mu(\vec{v}_{gr}\cdot\vec{k}) > 0$, where $\vec{v}_{gr} = 2c^2\vec{k}/[\partial(\omega^2 n^2)/\partial\omega]$ is the group velocity. Thus, $\mu > 0$, if $\vec{v}_{gr}\cdot\vec{k} > 0$, and $\mu < 0$, if $\vec{v}_{gr}\cdot\vec{k} < 0$. Similarly, for the density of the electromagnetic energy of the p-waves (the magnetic field is polarized in z direction), we find $\varepsilon > 0$, if $\vec{v}_{gr}\cdot\vec{k} > 0$ and $\varepsilon < 0$, if $\vec{v}_{gr}\cdot\vec{k} < 0$. In other words, in order to obtain propagating electromagnetic waves, both ε and μ should have the same sign that is in fact negative at the Γ point of the first band.

The band spectrum at the Γ point of band 1 can be written as $\omega^2 = \omega_1^2 - \alpha c^2 k^2$, where α is a parameter close to 1. Numerical calculations[40] provide $\alpha = 0.94$ for the lattice of Figure 10. It follows from the wave equation, that if $\varepsilon\mu\omega^2 = c^2k^2$, then

$$\varepsilon\mu = \frac{1}{\alpha}\left(\frac{\omega_1^2}{\omega^2} - 1\right) \tag{27}$$

i.e., $\varepsilon\mu > 0$ for $\omega < \omega_1$. From the band calculations[40] one may determine the effective constants:

$$\begin{aligned} \varepsilon &= -1.2 \\ \mu &= 0.89\left(1 - \frac{\omega_1^2}{\omega^2}\right) \end{aligned} \tag{28}$$

It should be noted that the simple consideration leading to Eq. (28) is the result of band repulsion at the Γ point. It fulfills at the band maximum where the simple relation $\omega^2 = \omega_1^2 - \alpha c^2 k^2$ holds, i.e., for $\omega_1 - \omega \le \Delta$, where Δ is the gap between the bands 1 and 2. Thus one has $|\mu| \le \Delta/\omega_1$.

The frequency dependence in Eq. (28) corresponds to the dispersion Eq. (8) presented by Veselago.[43] More general expressions for ε and μ were proposed by Pendry,[22] Shelby and co-workers:[44]

$$\begin{aligned} \varepsilon &= 1 - \frac{\omega_{ep}^2 - \omega_{e0}^2}{\omega^2 - \omega_{e0}^2 + i\gamma\omega} \\ \mu &= 1 - \frac{\omega_{mp}^2 - \omega_{m0}^2}{\omega^2 - \omega_{m0}^2 + i\gamma\omega} \end{aligned} \tag{29}$$

where ω_{ep} and ω_{mp} are the electric and magnetic plasma frequencies, ω_{e0} and ω_{m0} are the low-frequency edges of the appropriate bands, and γ is the damping factor.

3.1. Self-Collimating in Photonic Crystals

The phenomenon of self collimation is due to a peculiarity of the band spectra of some PhCs. Figure 11a from the paper[45] represents photonic bands of the first two bands of a Si slab patterned with cylindrical holes arranged on a square lattice. The Figure 11b and 11c represent the equifrequency contours of the first (b) and second (c) bands. As one can see, both contours can be approximated by squares. What follows from such an approximation? Let us consider a light beam incident on a PhC slab. The tangential field components should be continuous at a plane PhC boundary. However, if this component is directed along the side of the square in the equifrequency contour [(111) for the band I or (100) for the band II], the direction of the group velocity $\nu_{gr} = \partial\omega(k)/\partial k$ (it is depicted by arrows in Fig. 11) does not depend on the angle of incidence. This means that the light beam being non-collimated outside the slab becomes collimated inside. Figure 12 illustrates this for point source illuminating the PhC slab. We see that the spherical wave outside the slab becomes nearly flat inside the slab. Self-collimation is not favorable for the "superresolution lens," but the effect can be used for the construction of small optical devices like waveguides, splitters etc.[47]

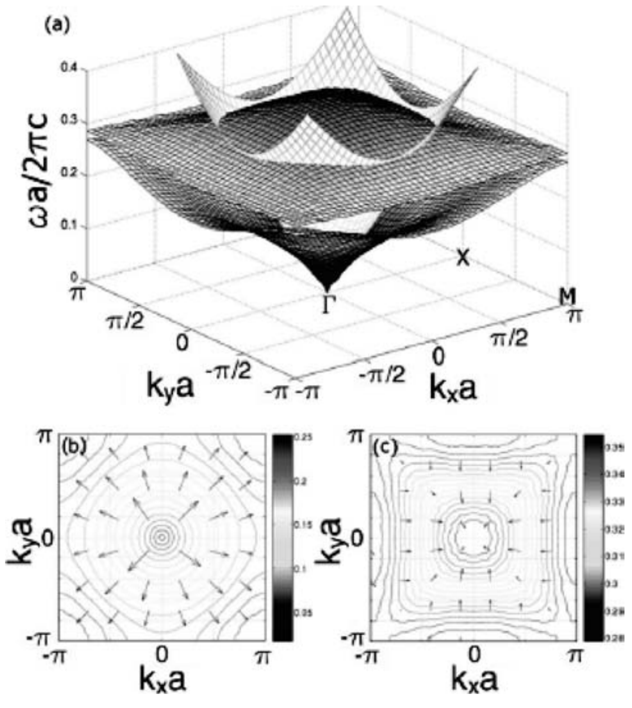

Fig. 11. (a) The dispersion, $\omega(k)$, for the first two bands of the square PhC. The light cone is represented as unshaded mesh. (b,c) The equifrequency contours for the first (b) and second (c) bands. The vectors represent the group velocity. Reprinted with permission from [45], J. Witzens et al., *IEEE J. Sel. Top. Quant. Electron.* 8, 1246 (**2002**). © 2002.

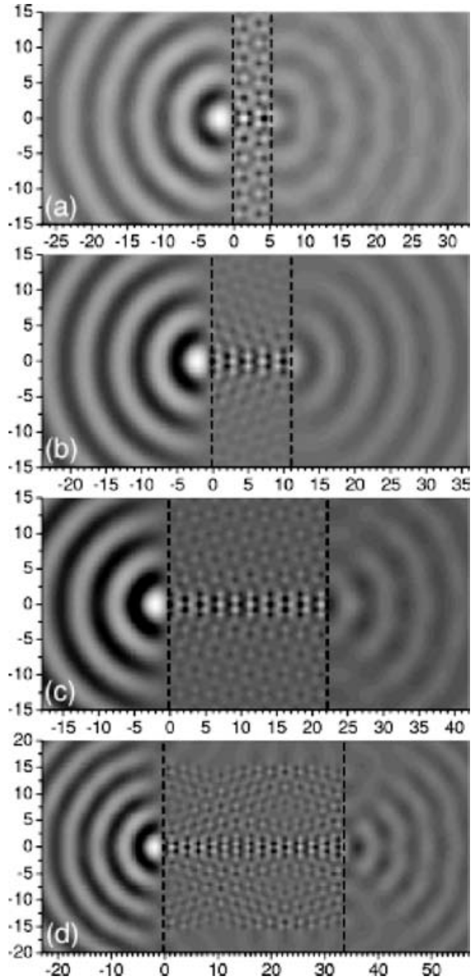

Fig. 12. Field modulus of a point source and its image across the (a) 8-, (b) 16-, (c) 32-, and (d) 48-layer photonic crystal slabs. Reprinted with permission from [46], Z.-Y. Li and L.-L. Lin, *Phys. Rev. B* 68, 245110 (**2003**). © 2003.

A rigorous theory of dipole imaging in PhCs has been developed.[48] This shows that the principal contribution to the far field of the dipole radiating in a PhC comes from the narrow regions of the equifrequency surface determined by the observation direction.

In the study[47] a PhC structure based on silver nano wires was used to avoid self-collimation. Far field imaging with the diffraction-limited resolution was achieved. However, sub-diffraction resolution is possible only in the

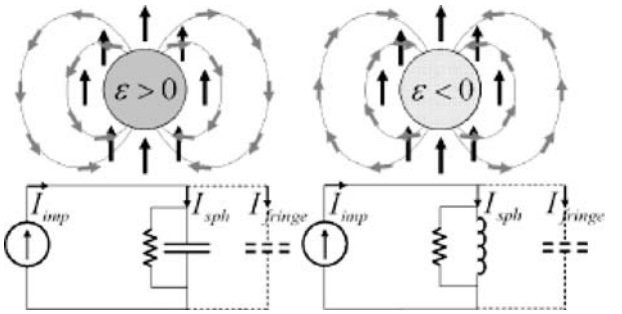

Fig. 13. Basic nanoscale circuits in the optical regime. Left: A non-plasmonic sphere with $\varepsilon > 0$ (nanocapacitor); right: A plasmonic sphere with $\varepsilon < 0$ (nanoresistor). Solid black arrows show the incident electric field. The thinner field lines together with the gray arrows represent the fringe dipolar electric field from the nanosphere. Reprinted with permission from [50], N. Engheta et al., *Phys. Rev. Lett.* 95, 095504 (**2005**). © 2005.

near-field region. Self-collimation of light in a 3D PhC has been considered.[49] In particular, woodpile and inverse opal PhCs were studied. FDTD calculations show that self-collimation occurs not only in high-index ($n \gg 1$), but in low-index materials as well.

3.2. Inclusions of Plasmonic Nanospheres; NIMs for Visible Light

The idea of using of nano size inclusions to change optical properties of common materials is rather new.[50] It is well known that dielectric permittivity of noble metals at optical frequencies is negative. This means that plasma frequency

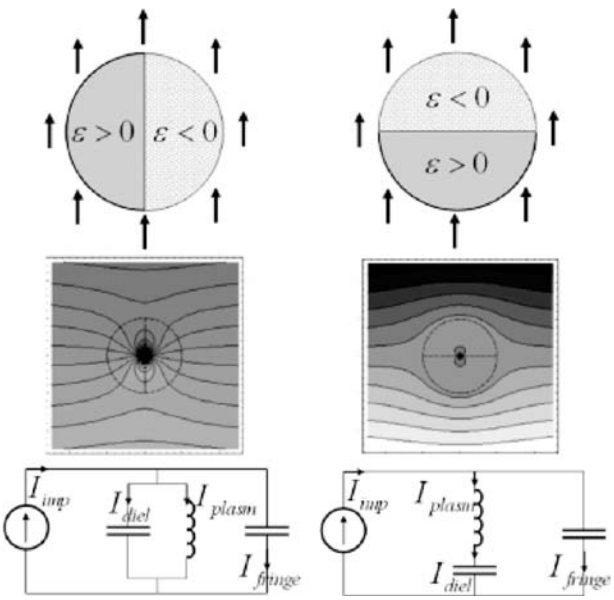

Fig. 14. Parallel and series nanoelements. Top: Two fused semicylinders illuminated by an optical field; middle: Potential distributions around and within the structure (solid lines show equipotential surfaces); bottom: Equivalent circuits showing parallel and series elements representing the fused structure as seen from the outside. Reprinted with permission from [50], N. Engheta et al., *Phys. Rev. Lett.* 95, 095504 (**2005**). © 2005.

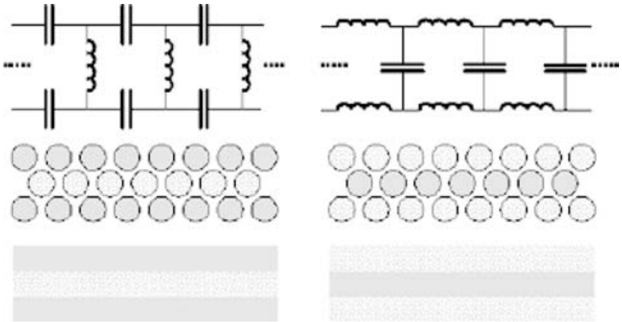

Fig. 15. Optical implementation of right-handed and left-handed nano-transmission lines. Top: Conventional RH and LH lines using the inductor and capacitor elements; middle: Plasmonic and nonplasmonic nanostructures playing the role of nanoinductors and nanocapacitors; bottom: Plasmonic and nonplasmonic layers may be envisioned to constitute layered transmission lines with forward and backward operation. Reprinted with permission from [50], N. Engheta et al., *Phys. Rev. Lett.* 95, 095504 (**2005**). © 2005.

ω_p of these metals exceeds the optical frequency ω as one may see from a simple, loss-free Drude model:

$$\varepsilon = 1 - \frac{\omega_p^2}{\omega^2} \tag{30}$$

The dielectric permittivity of dielectric materials is positive. Apparently, ordered structures composed of nano spheres with different permittivity ε could essentially change the properties of the metamaterial. Engheta and co-workers[50] have shown that a nano sphere of a material with positive ε illuminated by a light wave ($\lambda \gg R$, where λ is the wavelength and R is radius of the sphere) behaves like a capacitor, whereas a nano sphere of a material with negative ε behaves like an inductor (Fig. 13). The composite particles then behave like the parallel or series circuits of these nano elements (Fig. 14). This finally allows one to compose compound circuits of such elements. The structures presented in Figure 15 are right-handed and left-handed metamaterials, i.e., RHMs and LHMs or NIMs.

4. NUMERICAL MODELING AND SIMULATIONS

For the design and analysis of NIMs, numerical Maxwell solvers are highly valuable for two kinds of tasks, (1) the detailed analysis of various configurations containing NIMs and (2) the design of metamaterials exhibiting a negative index of refraction in a certain frequency range. These two tasks have special challenges. First of all, it is known from theory that the material properties of NIMs are dispersive, i.e., frequency dependent. Therefore, task 1 can only be handled with codes that can be applied to dispersive materials. Secondly, metamaterials with negative index of refraction that are currently fabricated exhibit periodic symmetries like crystals. In most cases, the cells of these metamaterials are arranged on a simple cubic lattice. Therefore, efficient simulations for task 2 require codes that can handle structures with periodic symmetries. In the following, we review the most prominent Maxwell solvers with a special focus on how they handle dispersive materials and periodic symmetries.

4.1. Available Maxwell Solvers

In electrical engineering, many different Maxwell solvers were developed in the early times of computers, i.e., before personal computers became a common tool for all scientists. Based on the most prominent methods, various commercial software packages were implemented. Such software packages are currently widely used in electrical engineering and in physics. Some of them were also used for the design and analysis of NIMs. Commercial software packages usually are black boxes tuned towards user-friendliness and efficiency for common engineering applications. Therefore, the estimation of the accuracy of the results is often cumbersome and the solution of special tasks may be tricky or even impossible. Namely periodic symmetries may not be handled efficiently by most of the commercial Maxwell solvers.

The standard formulation of Maxwell's equations in engineering separates time and space. Therefore, it is natural to distinguish Maxwell solvers depending on how they handle time and space. All early Maxwell solvers assumed harmonic time dependence, i.e., they worked in the frequency domain. Such frequency domain solvers work with a complex notation of the electromagnetic field and typically lead to complex matrix equations obtained either from a discretization of the entire space (domain methods) or from a discretization of the boundaries between domains with homogeneous material properties (boundary methods). Handling dispersive, i.e., a frequency dependent material is trivial for such methods and periodic symmetries provide no essential problems because the Bloch and Floquet modes of periodic structures are also defined in the frequency domain.

In 1966 Yee[51] proposed the first time domain code based on a finite difference scheme. At this time, computer resources (memory and speed) were not sufficient for solving even relatively simple problems with Yee's Finite Difference Time Domain (FDTD) method. With growing computer power, FDTD became—because of its simple concept and implementation—the most prominent technique. Furthermore, time domain variants of techniques other than finite differences were developed.

4.1.1. *Time Domain Solvers*

Maxwell's equations in the original form contain simple, first order time derivatives. From an approximation of the time derivatives by finite differences one immediately obtains a method to compute the field at a certain time t from the field at previous times, for example, $t-dt$, $t-2dt$, etc., where dt is the finite time increment. Depending on the order of this finite difference approximation of the time dependence, one (first order), two (second order), or more previous time steps are required. Yee's FDTD scheme uses the so-called leap-frog algorithm that has second order with the same computational costs as a much more inefficient first order scheme. This makes the Yee scheme very powerful. Prominent FDTD packages are XFDTD,[52] OptiFDTD,[53] Fullwave,[54] and Empire.[55]

Later, the Finite Integral Time Domain (FITD)[56] was developed based on the integral form of Maxwell's equations. Prominent FITD packages are MAFIA[57] and Microwave Studio.[58] The advantage of FITD is a simpler derivation of schemes for irregular space discretizations, but these are rarely used in practice because these schemes either destroy the second order accuracy of Yee's leap frog scheme or cause much higher computational costs. However, there is no essential difference between standard FITD and FDTD codes.

The Finite Elements Method (FEM)[59] is an old technique based on space discretization with unstructured meshes. It was first used for other disciplines of physics and closely related to variational integral formulations. In electrodynamics it became highly attractive when vector elements were introduced. It is important to note that time domain versions of FEM use a finite difference approximation of the time derivatives, i.e., the handling of the time is essentially the same as for FDTD. Frequently used FEM implementations are HFSS,[60] Maxwell3D,[61] and FEMLAB.[62]

Finite Volume Time Domain (FVTD) is a relatively new time domain technique that was originally introduced in fluid dynamics.[63] This method is based on the volume integral formulation of the curl and div operators in the Maxwell equations and works on unstructured grids. It is therefore very close to certain FEM implementations. To our knowledge FVTD was not yet applied to NIM problems.

The Transmission Line Matrix (TLM)[64] method is a prominent technique in computational electromagnetics that essentially replaces field domains by networks of transmission lines. This has advantages when microwave circuits with lumped elements are simulated. For NIMs, special transmission lines were designed and implemented in the commercial code MEFiSTo-3D.[65]

Finally, the Method of Moments (MoM)[66,67] is based on well-known Green's function techniques. Its advantage compared with the previously outlined methods is that only the domains that contain field sources (namely currents and charges) need to be discretized, which removes problems caused by the discretization or truncation of infinite space. Therefore, no Absorbing Boundary Conditions (ABCs) are required in MoM implementations. As a consequence, the MoM system matrices become smaller, denser, but not very well conditioned. The bad matrix condition causes severe stability problems for time domain versions. For this reason, currently no commercial time domain version of MoM is available.

All time domain solvers exhibit considerable problems with frequency dependent, dispersive materials. Taking these into account by using convolution integrals causes heavy and inefficient codes. Furthermore, the stability of iterations in time strongly depends on the material properties. For example, simple lossy material models with constant negative permittivity and permeability lead to instability. Therefore, all prominent time domain codes either do not handle dispersive materials or contain simplified material models such as the Drude[67] and Lorentz model that only provide a reasonable approximation within a sufficiently narrow frequency band. It is important to note that—depending on the model parameters—also such material models may cause instability. Thus, finding appropriate model parameters for a NIM is not trivial.

Since NIMs became very fashionable, Drude and Lorentz models were also implemented in some commercial codes, namely, XFDTD[52] and Empire,[55] whereas others (MAFIA[57] and Microwave Studio[58]) only contain dispersive material models for the permittivity but not for the permeability. As mentioned above, the TLM code MEFiSTo-3D[65] uses a different approach for modeling NIMs. In this approach, no explicit dispersive model for the permittivity and permeability is used. Instead, the material is approximated by lumped element circuits.

Not only dispersive material properties but although periodic symmetries of crystal-like structures considerably increase the complexity of time domain implementations. Since periodic symmetries are not present in most of the engineering applications, proper implementations of such symmetry conditions are often missing in commercial codes. If so, only special cases may be handled with Perfect Electric Conductor (PEC) or Perfect Magnetic Conductor (PMC) walls. Therefore, brute-force solutions are often considered when periodic symmetries are present, i.e., only a finite block of a metamaterial with a relatively small number of cells in each direction is modeled. This leads to time-consuming simulations of limited accuracy.

4.1.2. Frequency Domain Solvers

Theoretically, frequency domain methods have no problems with dispersive materials and periodic symmetries, but the latter are often not implemented in commercial codes because the interest in such structures is not high enough in standard electrical engineering. Furthermore, admitting negative values of the permittivity and permeability that is essential for the NIM analysis requires a careful implementation of numeric details. As a consequence, some codes do not accept negative values for the permittivity and permeability. For these reasons, frequency domain solvers are currently much less frequently used for NIM simulations although they should be much better suited than time domain codes.

Frequency domain solvers may be based on the same concepts as time domain codes, namely finite differences, finite elements, TLM, and MoM. Commercial frequency domain MoM codes are NEC,[69] MiniNEC,[70] FEKO,[71] and EMCoS.[72] To our knowledge, these codes were not used for NIM simulations up to now. Finite volume frequency domain codes are currently not available. Finite differences and TLM is much less often used in the frequency domain than in the time domain. Therefore, no important NIM simulations were carried out with such codes.

It has been mentioned, that MoM has considerably more dense system matrices than the other methods outlined above. As a consequence MoM is almost always used in the frequency domain. A further densification of the system matrix is obtained from boundary methods, namely the Boundary Element Method (BEM)[62,73] and Generalized Multipole Techniques (GMT).[74] The former is closely related to FEM, whereas the latter contains several "semi-analytical" techniques that will be outlined below. Boundary methods are exclusively used in the frequency domain and exhibit no problems with dispersive materials and periodic symmetries.

4.1.3. Domain Methods

Domain methods discretize the entire space. Because of limited memory, the open space must be truncated. This is done trough Absorbing Boundary Conditions (ABCs)[75–78] and similar techniques. Although the ABCs usually take only a small fraction of the computation time, they are essential for the quality of the results. For domain methods with unstructured meshes (FEM and FVTD), the mesh can often be truncated in such a way that the field propagates nearly perpendicular to the (truncation) boundary. In this case, even relatively simple ABCs perform well. For FDTD and FITD with structured meshes a breakthrough came with Berenger's Perfectly Matched Layer (PML)[79] technique.

For crystal-like metamaterials with periodic symmetries, a single crystal cell may be separated from its neighbor cells by means of fictitious boundaries with periodic boundary conditions.[76,81] As a consequence, the computational domain becomes finite and no ABCs are required.

The domain discretization leads to grid cells or elements with an electromagnetic field that is only coupled with a few neighbor cells or elements. Consequently the system matrix becomes sparse but relatively big. Big sparse matrices are best solved iteratively—provided that their condition number is low enough. Since the time discretization provides implicitly an iterative scheme, the time domain solution of domain methods becomes very powerful. It should be mentioned that the sparsity becomes more pronounced for large 3D problems than for smaller 2D problems (i.e., 3D with cylindrical symmetry). For this reason, time domain implementations of domain methods are the first choice for solving large 3D problems.

REVIEW

The MoM was originally designed as a pure domain method, but many MoM implementations are dedicated to idealized, loss-free problems composed of perfect conductors and dielectrics. As a consequence, the field sources (currents and charges) are located only on the borders of the field domains and only these borders need to be discretized. For periodic structures appropriate periodic Green's functions[81] may be introduced which allows one to only model a single, finite cell of the entire structure. Such MoM codes then behave very much like boundary methods. They would be well suited for the analysis of idealized metamaterials such as split-ring resonators arranged on a cubic lattice but surprisingly, MoM codes are currently rarely used for the simulation of metamaterials.

4.1.4. Boundary Methods

Boundary methods discretize only the boundaries between domains with homogeneous material properties. Therefore, these methods are restricted to problems with piecewise homogeneous material properties. They are characterized by relatively small, dense matrices that tend to high condition numbers. Such matrices are best handled by direct matrix solvers. Consequently, boundary methods are most powerful for not too complicated geometries and especially for 2D problems. To our knowledge, all boundary methods implementations work in the frequency domain.

Boundary methods may be subdivided in different types depending on how the continuity conditions on the boundaries are fulfilled. Boundary Element Methods (BEMs) approximate the given boundaries by polygons (in 2D), by triangular patches (in 3D), or by more complicated boundary elements. This automatically introduces some errors in the model. Other methods minimize the integrals over the weighted residual along the boundaries. Depending on how they evaluate these integrals, they can be considerably more accurate.

In boundary methods, the field in each homogeneous domain is approximated by a series of field (basis) functions that are analytic solutions of the Maxwell equations. Thus, boundary methods are close to analytic solutions and can provide highly accurate results when the boundaries are not discretized too roughly. For a proper selection of the basis functions in combination with the method of weighted residuals, the convergence essentially depends on the geometric properties of the boundaries: The higher the order of continuous derivatives of the boundaries, the faster the convergence. For infinitely many times differentiable boundaries, exponential convergence can be obtained. Such boundary methods may be called "semi-analytic." Especially for studying critical new concepts, such methods are of high value when no analytic solutions are available.

Many different boundary methods were developed by the scientific community: BEM,[59] the Multiple Multipole Program (MMP),[74,81,82] the Method of Auxiliary Sources (MAS),[83] the Method of Fictitious Sources (MFS),[84] The Discrete Source Method (DSM),[85] SPerical Expansions (SPEX),[86] T-matrix,[87] etc. Although these methods exhibit no severe problems with dispersive materials—as all frequency domain codes—and are often used for grating and photonic crystal problems with periodic symmetries, they are currently not often used for the design and analysis of NIMs. This may have several reasons. (1) The implementation of efficient boundary methods is rather demanding. (2) Flexible implementations (for example, MaX-1[88,89]) provide many features that require a profound analytical knowledge of the user and therefore are much less "user-friendly" than FDTD and FEM codes. (3) No prominent commercial codes are currently available.

4.1.5. Special and Auxiliary Methods

Periodic metamaterial structures for photons—including photonic crystals—are closely related to natural electronic crystals that were intensively studied in physics. Methods that were originally designed for solving the Schrödinger equation for periodic structures can also be applied for solving the Maxwell equations for periodic structures. Typical examples are Slater's Augmented Plane Wave (APW) method[90] and the Korringa Kohn and Rostoker (KKR) technique.[91] Note that these techniques are closely related.[92] Using plane waves for describing periodic problem is very natural. The Plane Wave Expansion (PWE) approach[93] essentially takes advantage of the special Fourier transform and is very useful for the computation of band diagrams[94] but limited to periodic structures. A PWE band diagram solver complements, for example, the commercial OptiFDTD[53] code.

4.2. Time-Domain Solutions of Configurations with NIMs

As soon as a metamaterial with negative permittivity and negative permeability, i.e., a NIM or a LHM exists for some frequency we can use it in combination with any natural material or with any other metamaterial. Codes that can handle NIMs can always also handle ordinary materials. Thus, the numerical analysis of arbitrary configurations causes no essential problem. However, currently almost all publications still focus on the simplest configurations of NIM prisms[95,96] and NIM slabs[95–102] because the details of these structures are still not well understood. The NIM prisms are mainly used in experiments for the verification of all-angle negative refraction. The corresponding simulations clearly demonstrate this and provide not much surprise. NIM slabs provide not only an exceptionally simple geometry but although very attractive physical properties, including super resolution. First, it was even assumed that NIM slabs may be considered as perfect optical lenses[27] which is in fact wrong. Since the debate on the resolution of NIM slabs is still ongoing and may be clarified by extensive numerical calculations, we focus on

REVIEW

the simulation of a NIM slab embedded in free space in the following.

Any NIM slab model is characterized by only a few parameters: Its thickness, its material properties, and the excitation. Therefore, it seems to be easy to provide an extensive analysis of the NIM slab. In fact, according to the NIM theory, any NIM must be dispersive. Thus, the description of the material properties and its handling in time domain codes become more difficult. Furthermore, since the slab extends to infinity, one must either truncate it or implement ABCs that can handle this special case. Since the latter is rather tricky, truncated 2D slab models of rectangular shape are considered in most publications. Thus, the width of the NIM slab is introduced as an additional parameter. Since a practical realization of the NIM slab also requires some truncation, this approach is also natural.

As mentioned before, the handling of dispersive material models through convolution integrals is cumbersome and numerically inefficient, except in very special cases that are usually implemented in such codes. Therefore, only Debye, Drude,[97] and Lorentz[98,99] models are considered in FDTD simulations of NIM slabs. These models contain only a few model parameters. For example, the Drude model is characterized by the plasma frequency and the collision frequency. Thus, one has 2 real parameters for describing the permittivity and 2 real parameters for describing the permeability in addition to the two geometric parameters (thickness and width). Additional parameters are then required for describing the excitation (plane wave, Gaussian beam, dipole, etc.). Note that even more parameters are required for realistic 3D models, for example, NIM disks of finite size.[103] Since the extensive study of problems with 6 or more parameters is extremely tedious, most publications consider 2D NIM slab models with identical Drude or Lorentz models for both the permittivity and the permeability, illuminated by a single source. Note that such models are not sufficient for obtaining reliable information on the optical resolution of the NIM slab.

Commercial codes often do not contain point sources that would be most reasonable for the study of the super resolution effect of NIM slabs. Therefore, point sources are usually approximated by small sources of small but finite extent. Incidentally, this also holds for domain discretization methods operating in the frequency domain. However, model truncation, approximation of the dispersive material model, and approximation of the excitation cause inaccuracies of numerical simulations.

The most attractive super resolution effect of the NIM slab is only observed well when the losses of the slab are sufficiently small and when the slab is impedance matched to the surrounding medium, i.e., free space. This means the relative permittivity and permeability of the slab must be close to -1. Usually, the Drude and Lorentz model parameters are tuned in such a way, that -1 is achieved for some frequency. The frequency range where the relative permittivity and permeability are sufficiently close to -1 is then very narrow. Thus, the time dependence of the excitation must be specified in such a way that its spectrum is very narrow. Therefore, smoothly ramped sinusoidal signals are usually considered. For obtaining steady state, usually extremely many iterations are required because slow convergence is observed, which is another source of inaccuracy and of long computation time.

Although time domain simulations are much less appropriate than frequency domain simulations, they provide interesting insight namely in the time evolution of the electromagnetic field. In the following a few essential time-domain results are outlined.

4.2.1. Finite Difference Time Domain (FDTD)

Figure 16 shows the electric field intensity at different time steps obtained from a FDTD simulation performed with the commercial XFDTD software package. A rectangular NIM area with height (thickness) $h = 1\lambda$ and width $w = 5\lambda$ is illuminated by a point source at a distance $d = 0.5\lambda$ from the upper boundary of the NIM rectangle. The location of the source is marked with O. The material is approximated by a Drude model in such a way that the relative permittivity and permeability are very

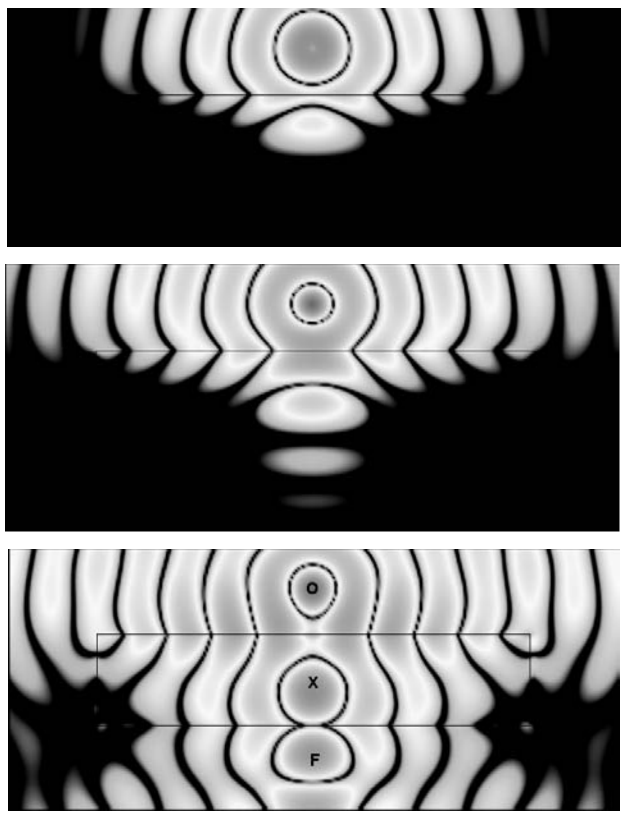

Fig. 16. Electric field intensity plot of an XFDTD simulation of a rectangular 2D NIM illuminated by a point source after 210 iterations (top), 310 iterations (center), and 930 iterations (bottom). The electric field is polarized perpendicular to the plane shown.

REVIEW

close to -1 for the main frequency of the signal (ramped sinusoidal time dependence). One can observe an almost circular wave front in the upper half space as expected because the NIM is impedance-matched to the surrounding free space and therefore no reflections are obtained. Inside the NIM one can observe a wave with negative propagation. It seems that the wave front here is much closer to the source. This impression is wrong. In fact, first much energy is pumped into the NIM and mainly in the area around its surface. As a consequence the field near the wave front inside the NIM (and in the lower half space) becomes relatively weak and therefore invisible in these automatically scaled plots. Therefore, it takes quite a wile until the focusing, i.e., the illumination of the area around the expected focus points X inside the NIM and F in the lower half space becomes visible. One can also observe that the illumination of the focus point F is first relatively broad and becomes more and narrower as time goes on. After 930 iterations, steady state is still not reached, but with more iterations one does not obtain essential new effects.

For finding out if this structure provides super resolution, the following must be done:

(1) steady state must be reached,

(2) the time average of the Poynting vector field must be evaluated,

(3) the illumination of the focus line (horizontal line through the point F) must be computed (The illumination is the component of the time average of the Poynting vector field perpendicular to the focus line.),

(4) the maximum illumination (in the point F) and the first local minima of illumination (corresponding to the first Airy rings) must be detected.

From this one obtains the distance d between the maximum of illumination and the nearest local minimum. Note that this is often considered as the resolution of the NIM slab. For the resolution defined by the Rayleigh criterion one then should consider a new model with two identical point sources at identical distance from the NIM surface and distance d between the two source points. Reaching steady state and the post-processing mentioned above is rather tedious for FDTD; therefore we omit this and postpone it to our frequency domain solutions.

4.2.2. *Transmission Line Matrix* (*TLM*)

Time domain TLM codes work with networks of transmission lines. Standard transmission lines may be approximated by lumped elements, namely inductors (along the line) and capacitors (parallel to the line). When capacitors along and inductors parallel to the transmission line are added, one obtains a TLM model for NIMs.[104–106] Such NIMs could in fact be fabricated in the microwave regime. It is important to note that the TLM model of NIMs is based on a possible realization rather than on a more or less ambiguous material model (Drude or Lorentz).

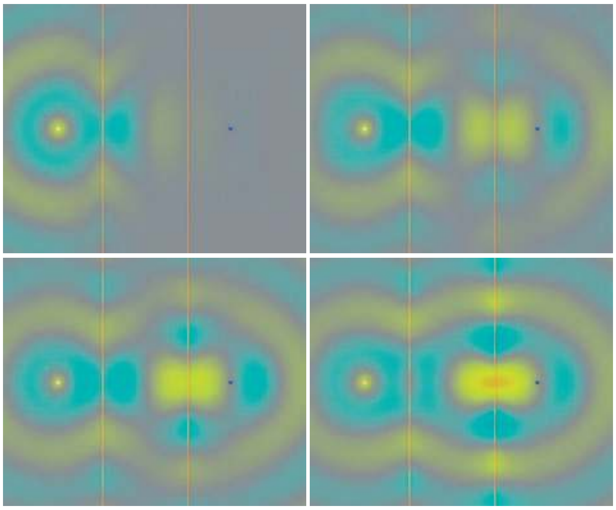

Fig. 17. Electric field intensity plot of an MEFiSTo-3D simulation of a 2D NIM slab illuminated by a point source to the left side, after 1 ns (top, left), 2 ns iterations (top, right), 5 ns (bottom, left), and 5 ns (bottom, right). The electric field is polarized perpendicular to the plane shown.

The NIM transmission line model consists of resonant circuits. The capacitors and inductors of this model are evaluated in such a way that the relative permittivity and permeability become equal to -1 for a certain design frequency. Because of the resonance characteristics, this model is very narrow banded and implicitly dispersive. Therefore, time domain TLM simulations need smoothly ramped sinusoidal input signals exactly as FDTD simulations. Losses my introduced in the TLM approach by adding resistors. For the following simulations with MEFiSTo-3D, no resistors are introduced, i.e., the models are loss free. Since MEFiSTo-3D contains absorbing boundary conditions that work well when the NIM surface is cut by the absorbing boundary, the slab needs not to be truncated. Figure 17 shows the corresponding results for four different time steps for a design frequency of 5 GHz. Also some differences to the FDTD results are caused by the different truncation of the model and by the different material models, the main effects remain the same, i.e., much energy is pumped into the NIM until focusing becomes visible and many iterations are required for reaching steady state. The latter may more easily be seen from time-averaged field plots as in Figure 18. The fact that the NIM model is very narrow banded may be seen from Figure 19 there the design frequency is different from the center frequency of the input signal. When the relative difference of the frequency is only 1%, one may observe substantial differences in the field plot.

4.3. Frequency-Domain Solutions of Configurations with NIMs

Because of the difficulties with material dispersion, stability of the time iteration schemes, slow convergence, and problems of post processing, time-domain codes are

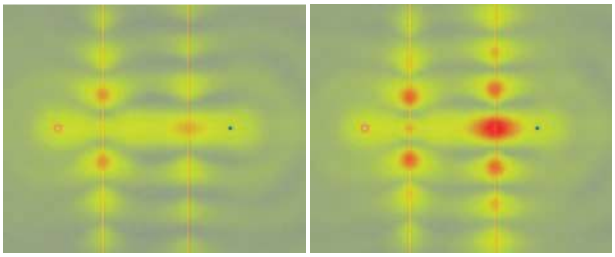

Fig. 18. Time average of the electric field intensity plot of an MEFiSTo-3D simulation of a 2D NIM slab illuminated by a point source to the left side, after 1 ns (top, left), 2 ns iterations (top, right). The electric field is polarized perpendicular to the plane shown.

not the best choice for the NIM analysis, except when one is interested in how the electromagnetic field in a NIM evolves in time after a light source has been turned on. Theoretically, all frequency domain codes can handle NIMs with negative permittivity and permeability, but in practice, there are several reasons why such codes might fail. This has to do with details of the implementations. Some implementations assume that the relative permeability of all materials is equal to 1, which causes considerably simplifications and faster performance of the code. Of course, such codes are useless for NIM simulations. Some implementations assume that all materials are loss free, which also causes considerably simplifications and faster performance. Unfortunately, heavy numerical problems may be observed in NIM simulations when the losses are set equal to 0. Therefore, such codes should also not be used.

4.3.1. Domain Methods

As mentioned before, all methods based on a domain discretization may be implemented either as frequency domain or as time domain methods. Since Finite Differences (FD) is most prominent in time domain (FDTD), one might expect that it is also most prominent in frequency domain (FDTD). In fact the success of FDTD is mainly due to Yee's leap frog scheme and its simplicity of implementation. In the frequency domain, FD is much less advantageous and therefore it is much less often used than its concurrent Finite Elements (FE). Prominent frequency domain codes that are often used for NIM simulations therefore are based on FE, namely HFSS,[53]

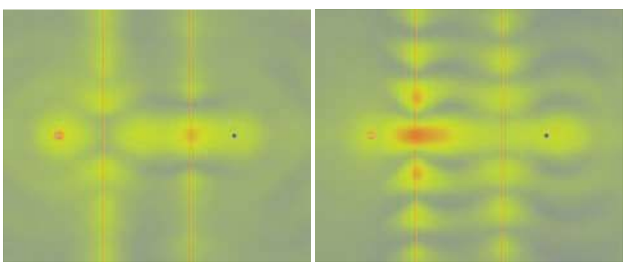

Fig. 19. Same as in Figure 18 for a design frequency that is reduced (left) or increased (right) by 1%.

Maxwell3D,[61] and FEMLAB.[62] The main reason for using FEMLAB[96, 101] is that it may be linked with MATLAB[107] codes for easily post processing the results. As mentioned above, this is important for studying the resolution of NIM slabs. It should be mentioned that FEMLAB, HFSS[108] and other FE codes may work in both time and frequency domain, but NIMs can only be handled in the frequency domain by these codes. Thus, the FEMLAB results presented by Lih et al.[101] are obtained from a frequency domain calculation although the authors claim that they used a FE time domain solver.

An important problem of all domain methods is the truncation of space. All commercial codes contain reasonable implementations of ABCs. Beside this, the main problem for FE and similar methods with structured grids is the generation of appropriate grids, i.e., meshes. All modern FE codes contain some automatic or even adaptive mesh generators. The quality of the results is heavily affected by the mesh generators. Figure 20 shows three different meshes obtained from FEMLAB the initial mesh is not sufficiently fine for obtaining accurate results, after 3 automatic mesh refinement steps, the mesh is fine enough but it huge, which affects memory requirement and computation time. As one can see, the mesh is more or less uniformly refined and not mainly in those areas where the field is strong, i.e., along the NIM boundaries and near the focus points X and F. FEMLAB allows the user to influence the mesh generation as also shown in Figure 20, but this is tedious work and requires some experience.

In addition to the mesh generator, the order of the elements and the matrix solver may heavily affect the accuracy of the results. Figure 21 shows that even advanced iterative matrix solvers (GMRES) may produce obviously wrong results. This considerably depends on the loss of the NIM: The smaller the losses, the more problems are encountered. When the loss tangent for the complex permittivity and permeability is below 0.01 inaccurate results are also obtained with the direct matrix solvers that are much more robust. Then, very fine meshes are required and the computation time becomes extremely long since it grows with the cube of the nodes of the mesh for direct matrix solvers. Furthermore, one can see that inaccurate results are also obtained for first order elements. Note that the sparsity of the FE matrix decays and the condition number increases with increasing order. Thus, iterative matrix solvers would work best for first order elements, but in this case the number of elements turns out to be too high for a computation on a personal computer.

Since post-processing is relatively easy with FEMLAB, we can also compute the illumination along the focus line (see Fig. 22). From this plot, one then can obtain the distance d from the maximum peak to the nearest local minima. As one can see from Figure 22, there is some noise due to the inaccuracy of the computation and this noise increases when the loss tangent decreases. Furthermore, the curves shown are not symmetric although the

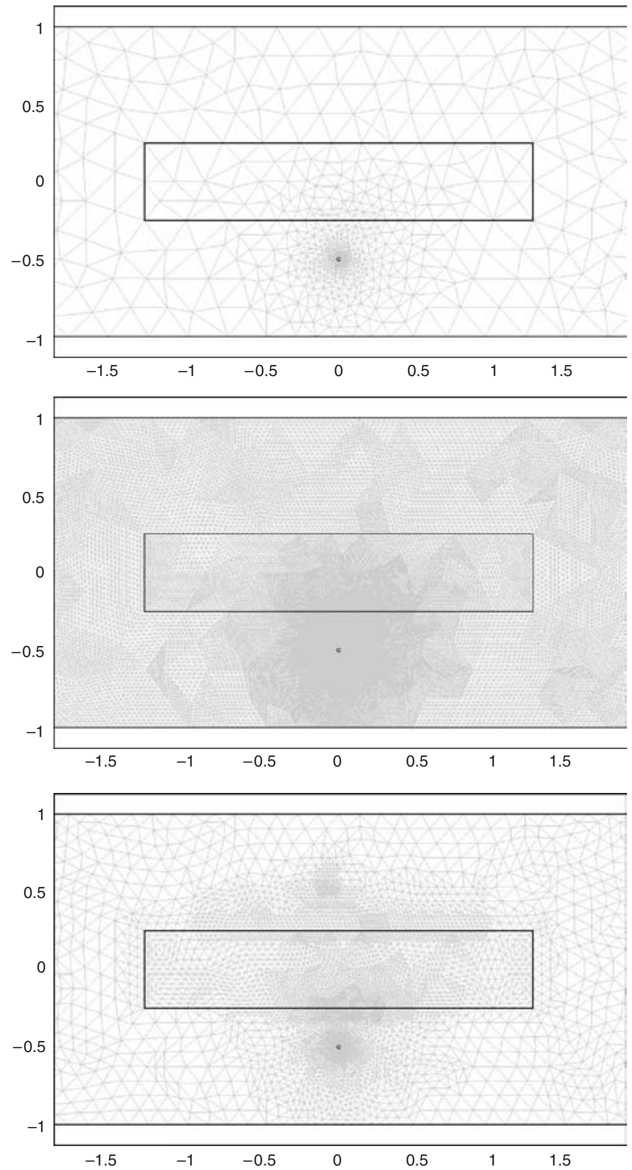

Fig. 20. Meshes for a rectangular NIM illuminated by a point source (below the rectangle) generated by the FEMLAM mesh generator. Top: Initial mesh, center: After 3 automatic mesh refinements, bottom with user-guided mesh refinement.

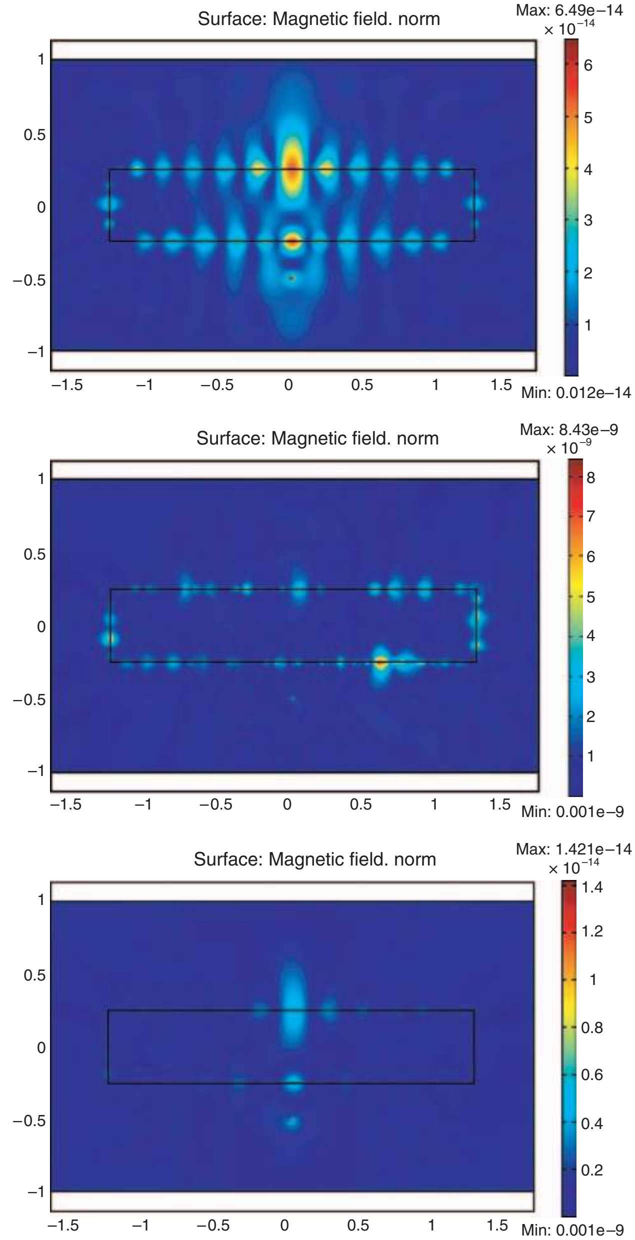

Fig. 21. Magnetic field intensity plot of an FEMLAB simulation of a 2D rectangular NIM illuminated by a point source near the bottom side. The magnetic field is polarized perpendicular to the plane shown. Top: Second order (quadratic) elements with direct matrix solver, center: Second order (quadratic) elements with iterative GMRES matrix solver, standard preconditioner, bottom: First order (linear) elements with direct matrix solver.

configuration is symmetric. This is also an effect of the inaccuracy of the results. Both effects cause difficulties when one wants to automatically extract d by some numerical procedure. When the noise is too strong, such automatic procedures detect local minims at completely wrong positions. For extensive studies of the resolution of a NIM slab depending on its size, shape, loss, etc., one therefore needs either extremely time-consuming FE models or one must invent and implement sophisticated post-processing procedures.

4.3.2. Boundary Methods

When one increases the order of finite elements, one can reduce the number of elements. As a result, the FE matrix becomes less sparse and its condition number increases, but at the same time, the accuracy of the result is increased when the matrix size is kept constant. Finally, one may obtain a single, high order element for each natural domain, e.g., one for the NIM and one for the space outside. This is nothing else than a boundary method. Boundary methods lead to very small, dense matrices that tend to be ill-conditioned. When the problem of the condition number is correctly solved,[81] these methods are superior to

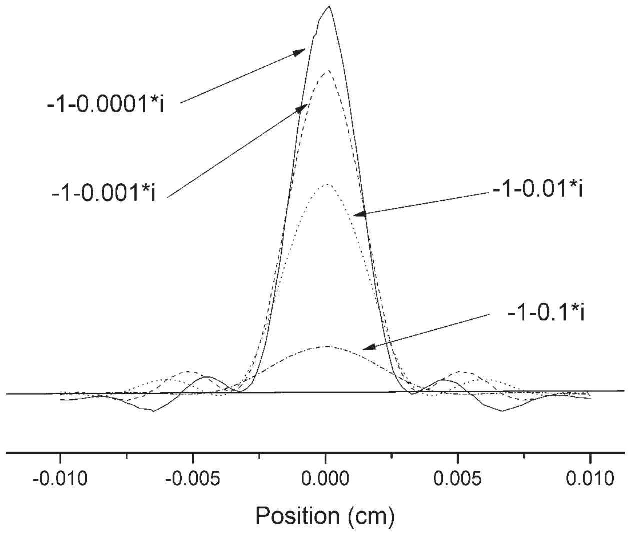

Fig. 22. Illumination (arbitrary units) along the focus line obtained for the NIM configuration shown in Figure 21. FEMLAB simulation for different loss tangents ranging from 0.1 to 0.0001.

domain methods as long as models with not very complicated geometry and linear material properties are considered and especially when high accuracy is desired. For the following results the MMP solver contained in the MaX-1 code[88, 89] is applied. This code also provides features for advanced post processing.

Figure 23 shows the time average of the Poynting vector field for a NIM slab with rectangular shape and with circular endings. Since the field along the NIM boundaries is strong even far away from the source, it is not trivial that the shape of the ending and the width of the NIM do not strongly affect its resolution. As one can see, the field near the endings strongly depends on the shape, but at some distance it is almost not affected. One also can see that the field intensity along the NIM boundary becomes very strong when the loss tangent of the NIM is small. Then, the field near the boundary may even be much stronger than near the focus point. This gives a hint to the problems encountered in the FEMLAB simulation.

For more extensive studies on the NIM slab resolution one best analyzes the illumination along the focus line, i.e., the time average of the Poynting vector component perpendicular to a line parallel to the NIM slab trough the focus point. Figure 24 shows the illumination for different cases with a single point source and with two symmetric point sources, for the electric field perpendicular to the cross section plane (shown in Fig. 23). For the other polarization (magnetic field perpendicular), one obtains identical curves because the relative permittivity is equal to the relative permeability for both the NIM and the surrounding free space. As one can see, the shape of the endings play almost no role (the corresponding curves overlap almost entirely) and the width of the NIM may be reduced to one half without a significant change of the illumination near the focus. Obviously, the NIM loss drastically affects the

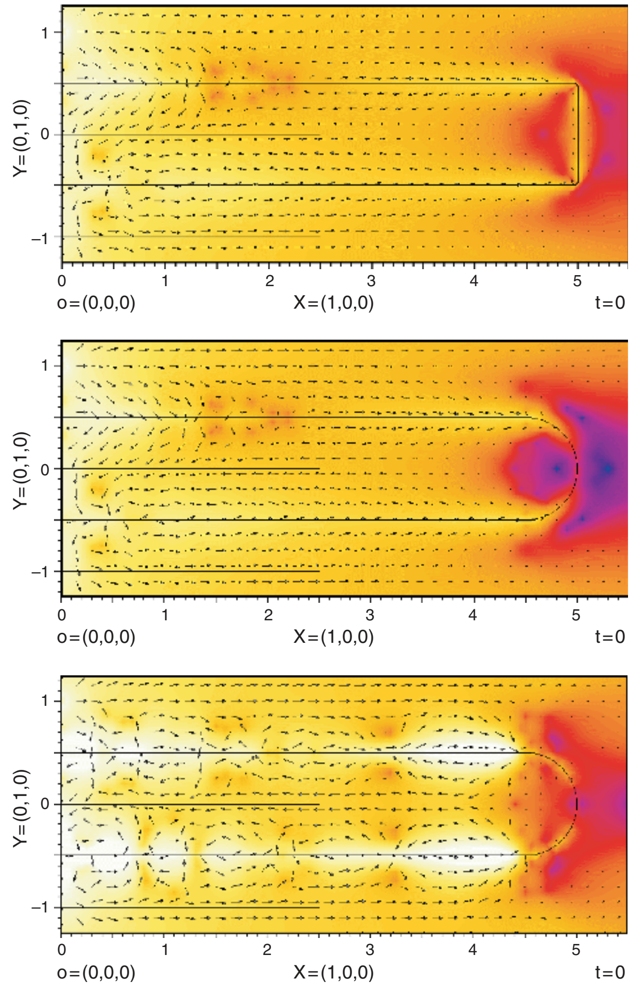

Fig. 23. Time average of the Poynting vector field of a MaX-1 simulation of a truncated 2D NIM slab illuminated by a point source to the tom side. The electric field is polarized perpendicular to the plane shown. Only the left half of the (symmetric) structure is shown. Top: Rectangular shape, loss tangent 0.01 (complex relative permittivity and permeability equal to $-1 * 0.01 * i$). Center: Circular endings, loss tangent 0.01. Bottom: Circular endings, loss tangent 0.0001. Arbitrary units are used for these plots. The wavelength is 1 (arbitrary unit).

absolute value of the intensity. From this, one can see that a strong absorption is obtained even for rather small loss tangents of only 0.01. Since the distance of the first local minimum to the center peak is also much affected by the loss tangent, it is obvious that the resolution of the NIM slab decays with increasing loss tangent.

It is remarkable that negative illumination is observed for some intervals. In these intervals, the focus line is illuminated from the wrong side, which indicates that energy flow from the lateral sides of the slab through the focus line and then turns back towards the slab in such a way that it again crosses the focus line, this time from the wrong side. The question now is whether the "first local minimum" of the illumination near the main peak is the local maximum of the negative illumination or the location of the zero illumination, when the resolution is defined using

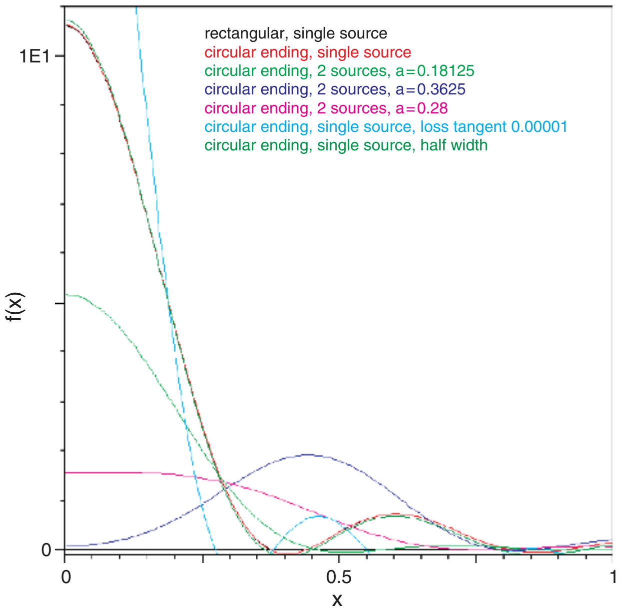

Fig. 24. Illumination (arbitrary units) along the focus line for the NIM structure shown in Figure 23. Black: Rectangular shape, single source, loss tangent 0.01. Red: Same as black with circular ending. Dark green: Same as red but width reduced to one half. Light blue: Same as red but loss tangent reduced to 0.0001. Green, magenta, blue: Same as red but 2 symmetric source points with different locations $x = \pm a$. Note that the distances between the symmetric sources are $d = 2a$.

the distance from the main peak to the nearest local minimum. The location of the zero illumination obviously leads to a smaller distance and therefore to a better value for the resolution. When we take the bigger value, i.e., $d = 0.3635$ for the NIM with loss tangent 0.01 and put two symmetric point sources at $x = \pm x_{\text{source}} = \pm a = \pm d/2$, we obtain an illumination along the focus line that clearly exhibits a single global maximum at the center point $x = 0$, i.e., from the illumination of the focus line one obtains the impression that there is a single points source only. When x_{source} is increased, the illumination peak becomes weaker and broader. For $x_{\text{source}} = 0.28$ ($d = 0.56$) one obtains a very broad peak. When a is further increased, two equal maxima are observed at $x = \pm x_{\max}$. This then indicates that there are two sources imaged by the NIM, but the distance between the image points ($d_{\text{image}} = 2x_{\max}$) is not equal to the distance between the source points ($d_{\text{source}} = 2x_{\text{source}}$). Instead of a linear dependence $x_{\max} = x_{\text{source}}$ (the magnification of the NIM slab is 1)—that would be expected for a "perfect lens"—one has a nonlinear function $x_{\max}(x_{\text{source}})$ that is shown in Figure 25. It can be seen that $x_{\max}(x_{\text{source}})$ approaches the line of perfect imaging ($x_{\max} = x_{\text{source}}$) with increasing x_{source}. The curves shown in Figure 25 offer different ways for definitions of the NIM slab resolution that are much more reasonable than the distance between the maximum of illumination and the first local minimum for a single point source. Note that also the distance between observed maxims of illumination[102] for extended objects or many point sources is misleading because of the

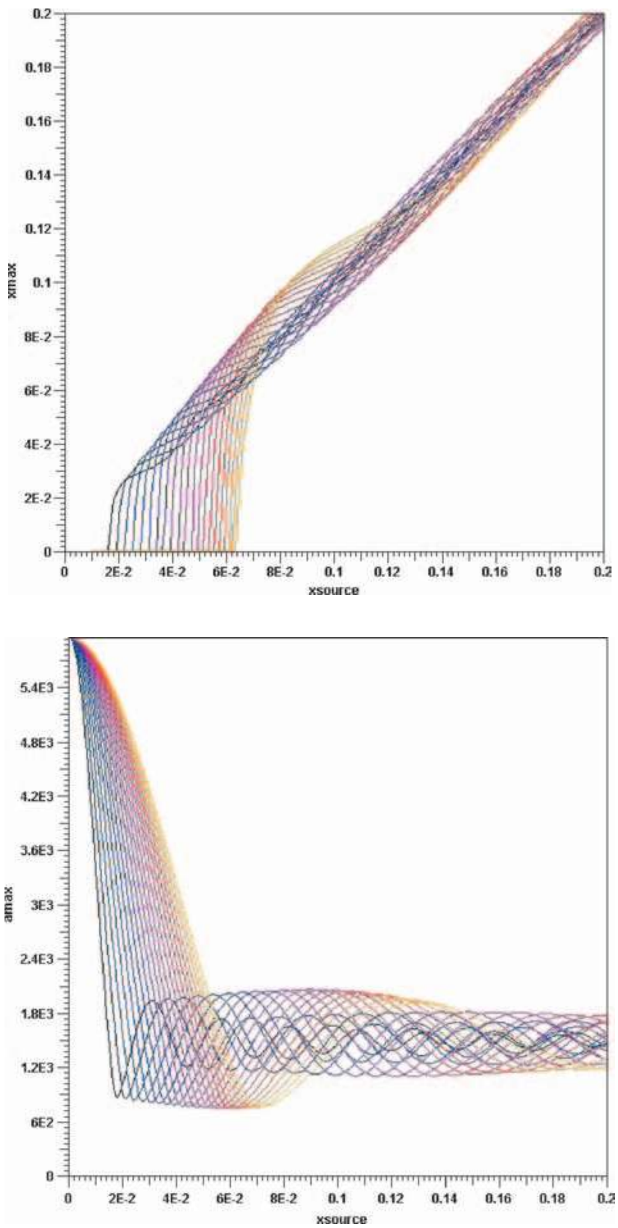

Fig. 25. Location $x_{\max}$ (left) and amplitude $a_{\max}$ (right) of the images (illumination peaks on the focus line) for the NIM slab shown in Figure 23, illuminated by two symmetric monopoles placed at $x = \pm x_{\text{source}}$. The Location and amplitude are given as functions of x_{source} for different wavelengths ranging from 0.5 (darkest curve) to 2.5 (brightest curve). As in Figure 23, arbitrary units are used.

nonlinear imaging properties (illustrated in Fig. 25 for 2 source points) caused by interactions between the sources and the NIM.

4.4. Design of Metamaterials with Negative Index of Refraction

In general, there are many ways to assemble metamaterials from "artificial atoms" that play the role of atoms in natural materials. For obtaining both negative permeability and permittivity, some resonance effect must be present.

Resonances are typically observed for "artificial atoms" that are not small compared with the wavelength. For shrinking the size of the "artificial atoms" one may take advantage of techniques used in electrical engineering for obtaining small lumped elements such as capacitors and inductors. For example, one can roll in a capacitor consisting of two thin metallic foils. This essentially leads to so-called Swiss rolls.[22] Such structures are only used at relatively low frequencies. At microwave frequencies, capacitors and inductors usually are fabricated with micro strip technology, i.e., as metallic structures on printed circuit boards. A famous microwave structure for obtaining NIMs is the split-ring resonator.[22] For obtaining a NIM one may assemble many Swiss rolls, split-ring resonators or more general micro strip structures that play the role of "artificial atoms." Theoretically, this should be in such a way that the orientations and locations of the atoms are somehow randomized when one wants to obtain an isotropic NIM that may be easily be described by a scalar permittivity and a scalar permeability. This is done, for example, when chiral metamaterials are fabricated by suspending arbitrarily oriented spiral antennas in some dielectric. The numerical analysis of such isotropic metamaterials is extremely demanding. Fortunately, NIM metamaterials usually consist of "artificial atoms" located on a regular (usually cubic) lattice like crystals. This drastically reduces the numerical analysis because only one lattice cell (primitive cell) needs to be modeled—provided that the numerical code can handle periodic structures using periodic Green's functions[81] or periodic boundary conditions.[80] In order to obtain isotropic metamaterial properties on needs at least three "artificial atoms" oriented in three perpendicular directions for each lattice cell.

Since NIMs at microwaves have periodic, i.e., crystal-like structure, it is natural to explore Photonic Crystals (PhCs) with respect to negative index properties. Here, it is important to note that the cell size of a PhC usually is not very small compared with the wavelength. Thus, near field effects occur in the vicinity of a PhC surface. These effects are not obtained from a simplified model that describes the NIM by macroscopic material properties like ordinary materials. This is very important for the analysis of thin NIM structures. For example, the resolution of a NIM slab is the better that thinner the slab is and the shorter the distances of the sources and of the focus line from the slab are.

Since the NIM slab performs the better the thinner it is, one finally can consider a slab that is thin compared with the wavelength. In this case, a quasi-static near field solution is sufficient. In quasi-static solutions, the electric and magnetic field components decouple. Therefore, it is sufficient for the electrostatic solution to have a negative permittivity only. It is well known that ordinary metals are described by a negative permittivity at optical frequencies, near plasmon resonance. It has been shown,[97,98] that super resolution might be obtained with a thin silver film, but in this case, the slab is no longer a metamaterial, it does not exhibit a negative index of refraction (therefore polarization plays an important role), and the configuration is closer to contact lithography than to optical imaging with a lens.

4.4.1. Split Ring Resonators and Swiss Rolls

The accurate numerical analysis of Swiss rolls with any Maxwell solver would be extremely difficult because it requires extremely fine discretization. Fortunately, approximate solutions may be derived.[22] However, since Swiss rolls may be used in practice only at relatively low frequencies—which leads to a large size of the experimental setup—split ring resonators and similar printed circuit structures operating at microwaves are much more attractive.

Split ring resonators consist of two metallic micro strip rings with a slit. They may have very different shape. Circular and square rings are most simple. Even these simple configurations have several parameters (width and height of the micro strips, distance between the rings, size of the slit, material properties of the rings, substrate, and surrounding medium) that need to be tuned in such a way that the desired NIM property is observed at some frequency. The split ring resonator may be considered as a small antenna that is responsible for the negative permittivity. A second (wire) antenna must be combined with for also obtaining negative permittivity. This contributes several additional model parameters. Because both antennas are resonant, the NIM becomes very narrow banded and the design and fabrication need to be highly accurate.

For the analysis of a single split ring resonator, first the FITD code MAFIA[57] was applied.[1] Later, a FDTD code was applied to the simulation of planar stacks of square split rings with wires.[111] Then, the FDTD code Fullwave[55] was used in conjunction with the Transfer Matrix Method (TMM) for a similar analysis with both circular and square split rings.[112] From the theoretical point of view, existing FITD and FDTD codes that do not contain implementations of periodic boundary conditions and cannot accurately handle thin metal strips, are certainly not the first choice. Brute-force computations with standard FDTD codes provide very limited accuracy that is not sufficient for the accurate analysis and optimization of NIMs based on arrays of split ring resonators and wire antenna. Currently, one therefore can still hope that much better NIMs may be designed by proper numerical optimizations, although these are expected to be extremely demanding.

4.4.2. Transmission Line Networks

NIMs made of split ring resonators and wire antennas may be considered as arrays of resonating antenna structures. An alternative is to fabricate arrays of resonating circuits

REVIEW

in a network of transmission lines.[102, 105] This does not only allow one to simulate NIMs using the TLM method but also to fabricate the corresponding transmission line networks using essentially the same technology of printed microwave circuits as for split ring resonators. Of course, it is most natural to simulate such circuits using TLM codes[106] such as MEFiSTo-3D.[65] Beside this the problems of structure optimization are the same as for split ring resonators.

4.4.3. Photonic Crystals

In 2000, anomalous refraction properties of Photonic Crystals (PhCs) were reported based on a numerical analysis with a transfer matrix method.[37] Later, 2D and 3D FDTD simulations were performed to analyze a PhC slab with all-angle negative refraction.[113, 114] In these simulations, the source was at a distance from the PhC slab that was shorter than the lattice constant. Therefore, channeling rather than isotropic wave propagation is observed in the PhC.[46] In a more careful study[115] superlensing of a PhC without the restriction of a short distance between source and PhC surface was demonstrated from numerical simulation. In this publication, the PWE approach[93] was usually used for the analysis of the band diagrams of the PhCs involved, but the finite PhC slab was then simulated using FDTD.

Since standard PhCs consist of two simple dielectrics with low loss, such configurations can be simulated with any numerical method for solving Maxwell's equations[116] and any commercial software described in this section.

The main problem of PhCs for superlensing is the lattice constant that is not much smaller than the wavelength, which certainly limits the resolution. By considering a PhC slab illuminated by two symmetric point sources, spatial resolution 0.4λ was reported.[115] Although this is encouraging, it is not really far away from the optical limit 0.5λ. Currently, it is not known how much the resolution of a PhC slab may be improved. This would require extensive simulations and optimizations. Since metals provide negative permittivity at optical frequencies "for free," also metallic and metallic-dielectric PhCs should be analyzed carefully as NIM candidates. For such investigations, frequency domain methods are favorable because they exhibit fewer problems with the dispersion of metals.

4.5. State of the Art

Currently, many different numerical methods and commercial codes may be used to analyze NIM structures and to design metamaterials with both negative permittivity and permeability. Despite of this, mainly simplified 2D models of a few NIM structures (namely, prisms, slabs, and simple lenses[108]) with a few specific parameters were published and extensive studies of 2D or even 3D NIM structures are still missing. Thus, only a few elementary effects are well known, but the potential of NIMs for practical applications with more complex geometry has not been explored at all. The main reasons for this are the high computational effort for complicated structures, the requirement of advanced post processing routines for extensive studies, and maybe also the lack of experience with commercial software of scientists. For the design of metamaterial structures with NIM properties, the situation is even worse. Here, optimizations based 3D models would be required for obtaining high quality metamaterials. Numerical optimizations may require the numerical analysis of thousands of different structures. Furthermore, optimization procedures are heavily disturbed by inaccuracies of the field solver. Thus, field solvers that are fast and accurate at the same time are required.

5. FABRICATION OF NIMS

The experimental concept to fabricate materials with negative permittivity at microwave frequencies from metallic wires was proposed by Pendry and coworkers in 1998.[21] In 1999, the same group[22] proposed to take advantage of the inductive response of collective motion (resonance) of electrons in non-magnetic conductive elements, so-called Split-Ring Resonators (SRRs), to also obtain negative permeability. This opened the way to NIMs.

Currently, we can distinguish two kinds of materials exhibiting a negative refraction: Composite MetaMaterials (CMMs) and Photonic Crystals (PhCs). CMMs exhibit simultaneously negative permittivity ($\varepsilon' < 0$) and permeability ($\mu' < 0$) within a certain frequency range. This immediately leads to a negative index of refraction ($n' < 0$). Dielectric PhCs are composed of materials with positive ε' and μ', but exhibit negative refraction because of peculiarities of dispersion characteristics at some frequencies.

5.1. Composite Metamaterials

CMMs consisting of artificially designed arrays of LC oscillators, mounted on electronic circuit plates, capable to interact with external electromagnetic fields, were first realized for frequencies around 10 GHz ($\lambda \approx 3$ cm).[117]

Two fabrication methods are used for the most of the CMMs exhibiting NIM properties: (a) combinations of conductive elements on a substrate and (b) Transmission Line (TL) configurations. The fabrication of CMMs with a negative index of refraction for 1D[1] and 2D[9, 44] propagation has been reported. First, the SRRs combined with straight wires were fabricated using printed copper circuits. The very specific geometry of the SRRs is shown in Figure 26. The splits in the rings provide resonance at a wavelength much larger than ring diameter and the smaller oppositely oriented ring inside the bigger one provides a large capacitance. When many SRRs oriented in three different directions in space and positioned on a cubic lattice, a metamaterial with effective permeability μ_{eff} is obtained.

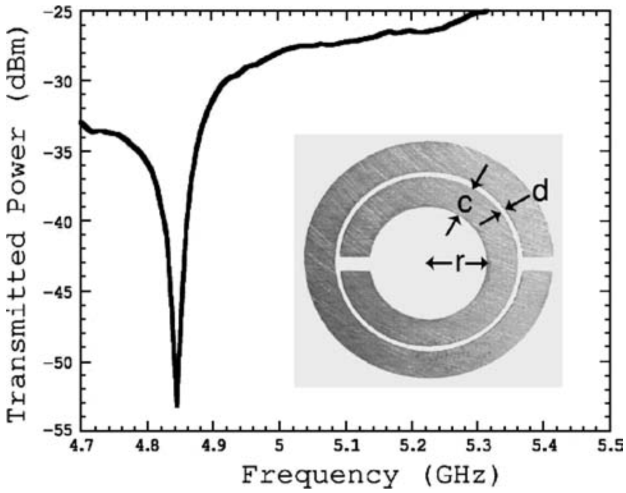

Fig. 26. Design and resonance curve of individual cupper split-ring resonator (SRR) for construction of 1D CMM. Resonance at ≈4.845 GHz was observed. Dimensions: $c = 0.8$ mm, $d = 0.2$ mm, $r = 1.5$ mm. Reprinted with permission from [1], D. R. Smith et al., *Phys. Rev. Lett.* 84, 4184 **(2000)**. © 2000, American Physical Society.

For μ_{eff} one obtains approximately:[22]

$$\mu_{\text{eff}} = 1 - \frac{F\omega^2}{\omega^2 - \omega_0^2 + iw\Gamma} \tag{31}$$

where F is the fractional area of the unit cell occupied by the SRR, Γ is the dissipation factor. For obtaining a NIM the SRRs are combined with a thin wire medium that provides negative permittivity.

Microwave scattering measurements were performed with a 2D square array of SRRs combined with wire elements fabricated with a period of 5.0 mm using commercially available materials. The 2D isotropy of this NIM was achieved by placing the SRR elements along two mutually perpendicular directions as illustrated in Figure 27.[9,44]

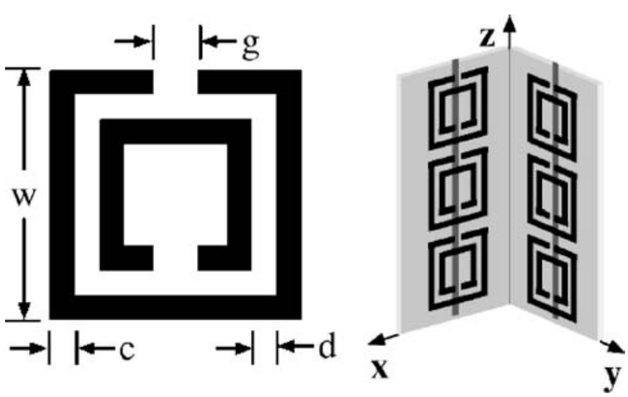

Fig. 27. Design of the unit cell of SRR used for construction of 2D CMM. Resonance at GHz was observed. Dimensions: $c = 0.25$ mm, $d = 0.30$ mm, $g = 0.46$ mm, $w = 2.62$ mm. Unit cell forms lattice constant of 5.0 mm and consists of 6 copper SRR and 2 copper wire strips (0.25 mm thick) mounted on 0.25 thick fiberglass G10 substrate. Wires are 1 cm long and located on the other side of substrate. Substrate plates make an angle of 90°. Reprinted with permission from [44], R. A. Shelby et al., *Appl. Phys. Lett.* 78, 489 **(2001)**. © 2001, American Institute of Physics.

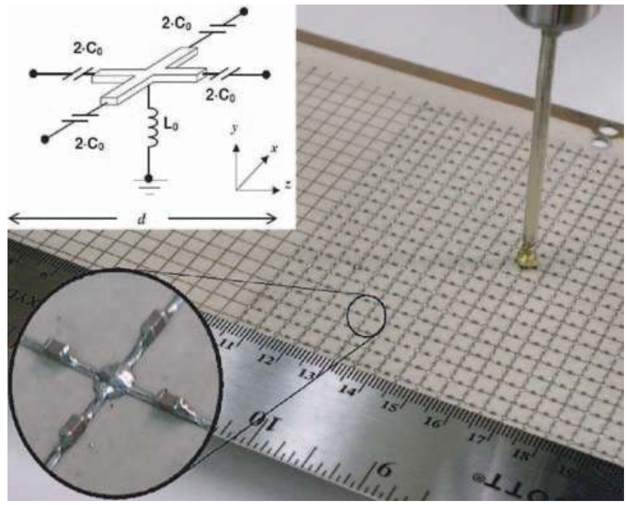

Fig. 28. Prototype of large periodically loaded TL CMM, containing two regions with negative index of refraction (21×40 cells, 105×200 mm) and PRI properties (21×21 cells, 105×105 mm). The square inset shows scheme of the unit cell of the size d for the 2D transmission line NIM material. The real unit cell structure is shown on the round insets. The near-field detection probe is also shown. This media may be considered as homogeneous if the unit cell constant d is much smaller than an external wavelength. Reprinted with permission from [119], A. K. Iyer et al., *Optic Express* 11, 696 **(2003)**. © 2003, Optical Society of America.

Other modifications compared to the first study[1] comprise the reduction of SRR dimensions for X-band microwave frequencies, the placement of wire strips behind substrate of the SRR, increase of the density of the thin wires to 2 per unit cell. Photolithography technique was used for printing the SRRs and the wire elements on the two sides of the substrate plates. It is important to note that the SRRs and the wire elements must provide negative permeability and negative permittivity at overlapping frequencies.[44]

The alternative principle of the Transmission Line (TL) approach and the corresponding equivalent material parameters $\varepsilon(\omega)$ and $\mu(\omega)$ are discussed in the paper.[118] The large periodic array[119] shown in Figure 28 is an example of this approach. The equivalent material parameters can be obtained from Eqs. (32):

$$\mu_N(\omega) = \mu_P - \frac{1/g}{\omega^2 C_0 d}, \quad \varepsilon_N(\omega) = \varepsilon_P - \frac{g}{\omega^2 L_0 d} \tag{32}$$

where μ_P and ε_P are the intrinsic material parameters of the host transmission line medium (that contributes to positive parameters of the NIM material). The reactive inclusions C_0 and L_0 describe negative frequency dependent contributions. The NIM unit cell consists of a microstrip grid loaded with surface-mounted capacitors and inductors embedded in the substrate. The whole device was mounted on a ceramic substrate ($\varepsilon_r = 2.94$) of height $h = 1.524$ mm and consists of regions with negative and positive index of refraction. Both media are built on a square grid of $w = 400$ μm wide microstrip lines with separations of $d = 5$ mm. The media may be considered as homogeneous if the unit cell constant d is much smaller than an external wavelength. The measured dispersion characteristics revealed a well-defined region of backward-wave propagation in the range from Bragg frequency (960 MHz) to approximately 2.5 GHz, exhibiting NIM properties, in good agreement with the predicted properties for the corresponding infinite structure, as shown in the inset of Figure 28.

An interesting approach for the verification of the regions of negative permeability and negative permittivity by a comparison study of the transmission spectra of CMMs fabricated using SRRs and CSRRs (closed split-ring resonators) was suggested.[120] SRR units made of thin copper layers on a circuit board with $\varepsilon = 4.4$ and thickness $d = 1.66$ mm were arranged in the following way to provide a rectangular lattice with lattice constants $a_x = a_y = 8.8$ mm, $a_z = 6.5$ mm: 5, 15, and 18 units along x, y, and z directions respectively.

Using a photo-proliferated process, the planar SRR microstructures on a 400 μm thick substrate were fabricated with LC resonance at $\lambda \approx 1$ THz ($\approx$300 μm wavelength).[121] The 3 μm thick Cu SRR elements formed a periodic structure with a lattice constant in the sub-wavelength range ($\lambda/7$, λ is the wavelength of external field at resonance frequency) to enable active properties.

Equation (31) provides the effective permeability for SRRs. Thin wire structures—with constrained electron transport along the 3D lattice—are characterized approximately by the effective permittivity

$$\varepsilon_{\text{eff}} = 1 - \frac{\omega_p^2}{\omega^2} \tag{33}$$

where the plasma frequency ω_p can be reduced to the infrared and microwave region by varying the concentration and thickness of the wires that form the lattice.[21, 122]

In practice, the metallic SRR element structures on a dielectric support may probably not be scaled down to achieve the NIM at infrared or even visible optical frequency. A new CMM design was successfully applied for the fabrication of a nanostructured array demonstrating strong magnetic activity and negative permeability in mid-IR.[123] This new CMM consists of arrays of nano-sized gold staples on a ZnS dielectric layer above a gold layer on a substrate. The unit cell size $a = 600$ nm is much smaller than experimentally observed resonance in the range of $\mu = 4$–7 μm. Interferometric lithography was applied for the growth of Au staples with a pitch grating of 600 nm. The ZnS was chosen due to its transparency for wave lengths between 2 and 10 μm. Modifications of the designed structure were studied: The reduction of the pitch to 180 nm, accompanied by a resonance shift to $\lambda = 1.30$ μm, and the change of the dielectric material (SiO_2) to further increase the capacitance.

Nanofabrication was used in order to fabricate metamaterials with LC resonance at $\approx$100 THz ($\approx$3 μm).[117] Gold single split-ring resonators with size $s = 320$ nm and thickness $d = 20$ nm were arranged on periodic square arrays with lattice constants $a = 450$–900 nm ($56 \times 56 = 3136$ SRR elements). All elements were smaller than the resonance wavelength of $\lambda = 3$ μm. Coupling of the electrical component of the external field with the capacitor leads to an excitation of the LC resonance at normal incidence. Comparisons of the transmission spectra with simulations indicate the frequency range where the magnetic field coupling with the LC resonance causes negative permittivity.

The realization of Pendry's idea[22] at visible light frequencies requires scaling the size of the unit cell down to 100 nm and the size of critical features down to approximately 10 nm, which is technologically extremely demanding, leaving questions on the interaction of visible light with material aside, which could result namely in too big losses. Nevertheless, Grigorenko and co-workers have succeeded to make an important step towards NIMs at visible frequencies.[124] Using high-resolution electron-beam lithography, they fabricated media on a surface area $S \approx 0.1$ mm^2 with negative permeability in visible using intrinsically non-magnetic material. The asymmetric plasmon resonance was created by a pairs of short Au pillars (Fig. 29) used as basic resonators, which is an essential simplification of the double split-ring geometry used at microwaves. Such simple resonator geometry may not only lead to loss reduction (due to a smaller number of resonant modes), but also opens the way to current lithography methods for the fabrication of NIMs in the visible range. After the optimization of the microfabrication process and preliminary numerical calculations, a non-cylindrical pillar shape leads to more efficient incident light coupling. At a lattice constant of $a = 400$ nm, Au pillars of height $h = 80$–90 nm and diameter of $d \approx 100$ nm were chosen. This cell geometry provides plasmon resonance at red light ($\lambda \approx 670$ nm). Furthermore, NIMs with other pillar geometries were also fabricated. The geometry was

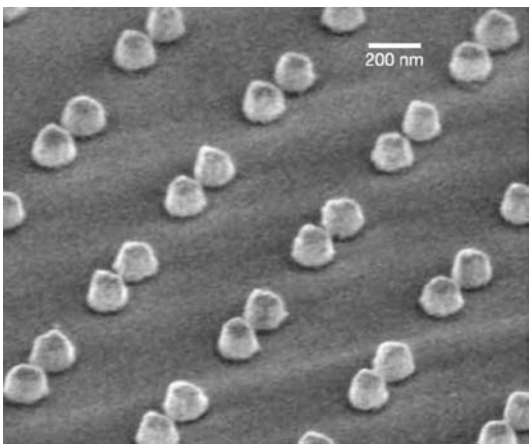

Fig. 29. SEM pattern of medium (array of Au pillars) with magnetic response at optical frequencies. Reprinted with permission from [124], A. N. Grigorenko et al., *J. Petrovic. Nature* 438, 335 (**2005**). © 2005, Nature Publishing Group.

optimized to provide efficient electromagnetic interaction within the pillar pair. The symmetric and anti-symmetric resonances for individual pillars and pillar pairs could be treated as plasmon resonances in nanoparticles. In the reflection spectra at normal incidence for TM and TE polarizations, "green" and "red" resonances are observed during the rotation of the samples, dependent on the structure of the fabricated media. As the authors have pointed out, though the fabricated structures exhibit both negative μ' and negative ε' within the same λ range (for example $\varepsilon' \approx -0.7$ and $\mu' \approx -0.3$ at the green resonance), but μ has a rather large imaginary component that prevented the observation of negative refraction.[124] Furthermore, a remarkable optical impedance matching effect was observed, which is characterized by the total suppression of the reflection from the interface between two media with different refraction indices. This leads to total invisibility of the structured films at green frequencies at TM polarization of the incident light.

5.2. Photonic Crystals

The negative refraction can be realized also with photonic crystals (PhC) that—in contrast to the CMMs—are inhomogeneous media with a lattice constants comparable to the wavelength. Although both ε and μ are positive in dielectric PhCs, typical NIM phenomena of negative refraction and superresolution can be expected from peculiarities of the dispersion characteristics of certain PhCs. The main advantage of PhCs over CMMs currently is that they can be more easily scaled to 3D and adapted to visible frequencies.[125]

Negative refraction at microwave frequencies was observed in both dielectric and metallic PhCs, for example, using a square array of alumina rods in air.[126] Transmission measurements confirmed negative refraction using the interfaces of the PhC in the Γ–M direction and indicated the maximum angular range of negative refraction at 13.7 GHz. 2D and 3D PhCs consisting of alumina rods were used for the demonstration of NIM in the microwave and millimeter wave ranges.[127] Two techniques, manual assembly of alumina rods and rapid phototyping, were used in this study for fabricating low-loss PhCs, investigated in the wave range from 26 GHz to 60 GHz. Negative refraction was shown both in FDTD calculations and transmission mode experiments on a 2D lattice.

Negative refraction in a metallic PhC with hexagonal lattice acting as a flat lens without optical axis (Pendry lens) at microwave frequencies was reported at 10.4 GHz for TM mode.[125] This PhC crystal consists of cylindrical Cu rods of the height $h = 1.26$ cm and radius $r = 0.63$ cm, with $r/a = 0.2$ (a is the lattice constant) forming a triangular lattice. Furthermore, cylindrical Cu tubes of the height $h = 60$ cm and outer radius $r = 0.63$ cm were arranged on a triangular lattice with the same r/a ratio of 0.2. Negative refraction was found for both TM and TE mode propagation, between 8.6 and 11 GHz (TM mode) and between 6.4 and 9.8 GHz (TE mode). Extensive experimental, band-structure, and simulations results were achieved,[125, 128] which opens the way to a variety of well tailored PhC structures. The advantages of metallic PhC were reported to be highest dielectric constants, low attenuation, and the possibility of focusing.[125]

An interesting PhC consisting of Al_2O_3 rods (dielectric constant $\varepsilon' = 9$, radius 0.316 mm, height 1.25 mm) on a square lattice with $r/a = 0.175$ and 0.35 was fabricated for measurements of lowering group velocity.[129] For the measurements of the group velocity ν_g, the PhC was arranged as parallel plate waveguide with TM mode and with electric field parallel to the Al_2O_3 rods. It was noted[119] that the negative refraction in this PhC proceeds in higher (valence) bands and does not interfere with the Bragg reflection and transmission efficiency.

The experimental demonstration of the light focusing due to negative refraction at infrared frequency was done using a PhC with air holes on a hexagonal lattice in a low-index contrast InP/GaInAsP/InP slab (lattice constant $a = 480$ nm, hole radius $r = 125$ nm) at the telecommunication wave length of $\lambda = 1.55$ μm.[130] The PhC pattern was fabricated using electron-beam lithography and chemical etching. The thickness of the InP top layer and intermediate layer is 200 nm and 420 nm respectively. Another example is a PhC composed of metallic resonators structured on a nanoscale.[122] A 2D unit cell consists of resonant structure with square Ag columns of side length $a = 600$ nm. An important point is that the external free-space wavelength at the resonance frequency is much larger than the length scale of the unit-cell dimensions. This allows one to consider the designed material as effectively homogeneous—which is not the case for usual PhCs. The negative permeability in these nanomaterials is confirmed by numerical simulations.

5.3. Applications

Many NIM concepts were suggested but only a few were realized up to now. One of the obvious reasons is the difficulty of the fabrication of artificial materials with sufficient homogeneity. Current NIMs rarely achieve a wavelength to structure unit ratio better than 10:1.[131]

The concept of composite right/left-handed (CRLH) metamaterials was suggested by Caloz and Itoh.[132] The transmission line theory (TL) approach for CRLH materials can be demonstrated by several already realized or at least simulated microwave applications:[132, 133] (1) Dual-band components capable to reduce the number of components in wireless communication systems. By replacing the $\lambda/4$ RH TLs of Branch Line Couples (BLCs) and ring couplers with CRLH TLs, the harmonic operational frequency limitation can be overcome. (2) New antennas include zero order resonance (ZOR) antennas of physical size less than $\lambda/2$ and 1D or 2D (depending on the unit cell structure)

REVIEW

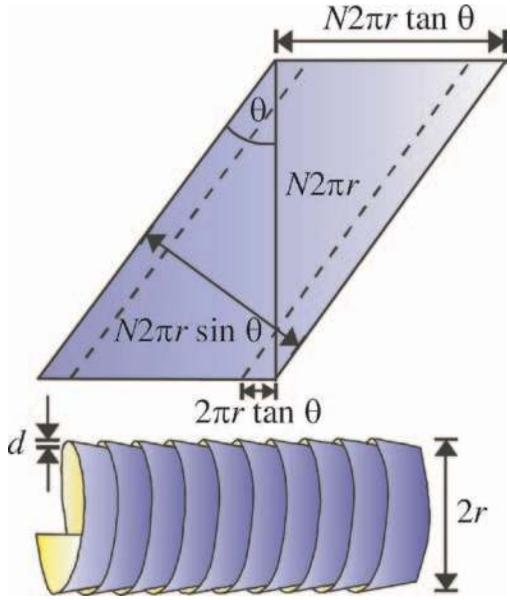

Fig. 30. Possible design for resonant chiral structure. Condition of strong chiral effect $\tan(\theta) \approx \pi r/\lambda_0$ at $r \ll \lambda_0$ leads to small values of θ. Reprinted with permission from [131], J. B. Pendry, *Science* 306, 1353 (**2004**). © 2004, Science Permissions Department.

frequency scanned Leaky Wave Antennas (LWAs) capable of continuous backfire-to-endfire scanning. The CRHL LWA radiates backward in the LH region and forward in the RG region with broadside radiation because CRLH TL supports an infinite wavelength with non-zero group velocity at the LH/RH transition point. (3) Both flat and curved microwave lenses that exhibit a negative refractive index at a certain frequency and that are not possible with RH materials can be realized by placing 2D CRLH metamaterials between two parallel RH plates.

The introduction of chirality might result in negative refraction of only one polarization. This could simplify the NIM design and lead to the extension of negative refraction field.[131] The example of practical realization of resonant chiral structure is shown in Figure 30.

New ideas on NIMs that are still on the level of concept formulation are worth mentioning because they may lead to principally new electromagnetic devices,[132] namely, an effectively homogeneous medium for backward-wave propagation, sub-wavelength diffraction, and enhancement of evanescent waves. The backward wave propagation in NIMs with opposite directions of the group and phase velocities provides interesting new applications including delay time filters and phase shifters from microwaves to optical frequencies.[129]

The fabrication of metamaterials with magnetic response at THz and optical frequencies can be used for such applications as compact cavities, adaptive lenses, tunable mirrors, security imaging, biomolecular fingerprinting, remote sensing.[121] Different elements like metallic wires and grids with the dimensions of order a wavelength are already used in the THz optics.

Low group velocities of c/50 (in a CMM) and c/10 (in two different PhCs) were measured experimentally.[129] The CMM, consisting of interleaved parallel arrays of SRRs and wire strips (WSs) was similar to those reported previously.[9, 44] The applied fabrication method of the Al_2O_3 PhC was described in Section 5.2. Earlier, slow ν_g of the order of c/3 had been observed in Si/SiO_2 and AlGaAs-based photonic crystals.[134, 135] The measured low ν_g (in the frequency window of 9.9–10.3 GHz for CCM, 7–8.5 GHz and 7.7–8.5 GHz for PhCs with different r/a ratio) can be explained by the character of the wave dispersion that can be determined from the band structure.[129] The key feature of the PhC band structure is the flattering of the band at the band edges, where ν_g is expected to be low. Strong reduction of the ν_g is due to strong modulation of the dielectric contrast (9:1 in fabricated PhC compared to 2.5:1 in colloidal polystyrene PhC). Even lower group velocities are expected for CMMs and PhCs with low transmission loss. The most important applications of low group velocity materials are delay line filters and phase shifters that are not possible with conventional materials.

Before discussing the experimental results of the flat NIM lens, illustrated in Figure 7, we come back to the question if the term “super lens” is really appropriate. As mentioned above and as pointed out earlier by one of the authors of this paper[129] the NIM slab does not correspond to the definition of a lens as an instrument of geometrical optics ($a > \lambda > \delta$, $a = b + c$). The “superlens” is rather some optical matching device that can transfer the image with size much smaller than λ from one point of space to another.[136] In the following, we are using the term “super lens,” keeping this in mind and remembering that the “super lens” effect only is observed when the width of the NIM slab is small enough.

The curved plano-concave lenses with negative index of refraction in the microwave range were designed using both types of NIM studied to date: CMM and PhC. The CMM lens with curved geometry was operating at 14.7 GHz. It consisted of metallic wires and SRRs assembled on a periodic cell structure (Fig. 31).[137] Good agreement between the simulation and measurement was reported.

The second example of an experimental NIM lens study is the imaging of far-field microwave radiation using a dielectric photonic crystal (PhC, Fig. 32).[138] A frequency-dependent negative refraction index $n(\omega) < 0$ was observed. Lenses with curvature radii of 13.5, 17.5, and 22 cm were implemented. The corresponding PhC consists of a periodic array of Al_2O_3 rods ($\varepsilon = 8.9$) in air, arranged on a square lattice with the ratio $r/a = 0.175$. Using equation $n = 1 - R/f$ (R is the radius of the curvature and f is the focal length), $n = -0.4$ at 9.25 GHz is obtained for this lens. Focusing by the a plano-convex lens was achieved for $n > 1$, $R < 0$, and for a plano-concave lens for $n < 0$, $R > 0$. NIM lenses have a larger radius of curvature for any value of $n < 0$ (stronger focusing characteristics) and correspondingly reduced aberration in the

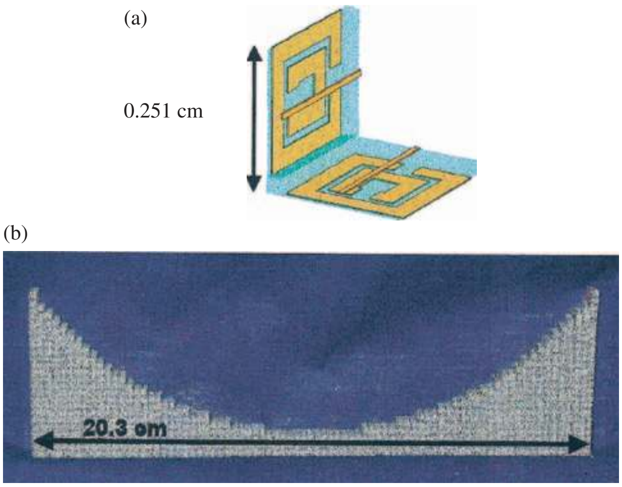

Fig. 31. Composite metamaterial (CMM) lens operating as optical element with negative index of refraction. Arrangement of 4 cells along x and varied thickness along y. The lens was fabricated in a cylindrical geometry. (a) Unit cell structure of lens based. (b) Plane-concave structure of the lens constructed from flat unit cells. Lens aperture is 20.3 cm, radius of curvature is 12 cm. Reprinted with permission from [137], C. G. Parazzoli et al., *Appl. Phys. Lett.* 84, 3232 **(2003)**. © 2003, American Institute of Physics.

image compared with positive index lenses. Besides, the NIM lens has much lower weight than a conventional lens of the same focal length what could be advantageous for space applications. Notice that the refractive index achievable in a PhC allows for further controlled change of the focal length and could lead to further reduction of the dimensions of the optical systems.[138]

It is important to note that the bandwidth of the PhC lens (2 GHz, or 22.7% of the operation range) is much larger than the bandwidth of the CMM lens, due to weaker dispersion.[138]

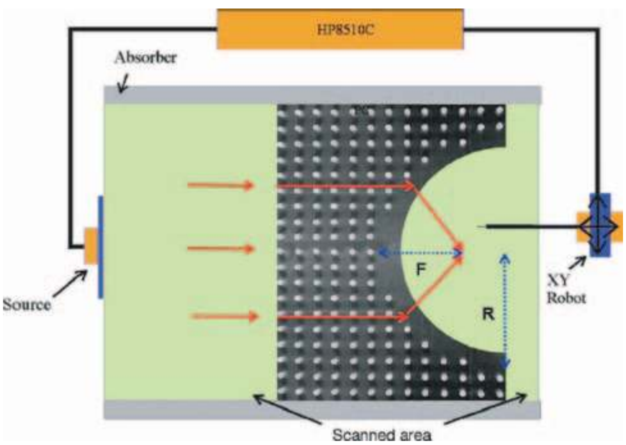

Fig. 32. Scheme of microwave focusing device (plano-concave lens) based on photonic crystal (PhC). An X-band waveguide, used as a microwave source, was kept at a distance of 150 cm from the flat lens surface. The sensor was mounted to a XY translation stage, scanning for the electric-field component of the relevant microwave range. Reprinted with permission from [138], P. Vodo et al., *Appl. Phys. Lett.* 86, 201108 **(2005)**. © 2005, American Institute of Physics.

Progress in the design of graded negative index of refraction (GRIN) lenses was reported.[139] Cylindrical and more complex spherical GRIN lenses were fabricated using a NIM slab with graded index of refraction at 17 GHz. Ray tracing calculations and MicroWave Studio simulations were used to determine the refraction gradient.

The difficulties in NIM design in infrared (IR) and visible light essentially limit the NIM applications. The limited success in the fabrication of optical LHMs was stressed also in the press-release "List of recent research results in the area of materials" by the EU network of excellence METAMORPHOSE.[140] The development of these fabrication methods was called as fundamental priority for device-based research in the field of materials organized for radio, millimeter wave and photonic super lattice engineering. Only a few of successful experimental results could be mentioned. One example is a periodic gold pattern with lattice constant 600 nm separated by a ZnS dielectric layer, showing resonance at ~55 THz (mid-IR).[123] In the second example,[110] the sub-diffraction-limited imaging with a silver super lens slab assisted by surface plasmon excitation was reported. The superlensing system in the second example has the following structure: 50 nm thick patterned Cr structure (illuminated by a plane wave) over a 40 nm thick PMMA spacer on a 35 nm thick Ag film (playing the role of the "super lens") that directly is placed on a 120 nm thick photoresist. Using UV light of $\lambda = 365$ nm, the image of 60 nm nanowires on 120 nm pitch was demonstrated, or $\lambda_0/6$ or $\lambda/4$—because the index of the PMMA, lens, and photoresist was close to 1.5. Note that a second PMMA spacer between lens and photoresist was missing. The calculated transfer function of this silver superlensing system allows to estimate, that a range of evanescent component from 2 to 4 k_0 can be enhanced and recovered by plasmon excitations. The thickness of silver layer d is of great importance: When $d >$ 40 nm, the enhancement is damped by material absorption. Although promising results were achieved, many questions are open: How can the observed significant losses be eliminated? What is the dependence of the transfer function on the thickness of the silver layer and on the PMMA spacers?

The phenomenon of superlensing becomes very promising, when considering the needs of increased optical storage density in digital recording and in the computer storage. These trends are obvious in the recent development from "red" (normal DVD, $\lambda = 650$ nm, NA $= 0.6$) to "blue" optical discs (BD, $\lambda = 405$ nm, NA $= 0.85$).[141] The necessity to use shorter wavelengths to increase the storage density can be illustrated by the diffraction limit problem: $\delta \approx \lambda/(n \sin \Theta_{max})^2 = \lambda/(\mathrm{NA})^2$, where δ is the depth of focus, n is refraction index of media, and NA is numerical aperture. The δ value corresponds to the diameter of the smallest resolvable mark. But the image resolution in conventional optical storage is limited by the diffraction limit

REVIEW

and search for new recording technologies is in progress. The application of "super lens" effects for high-density optical near-field recording with no diffraction limitation was first considered in the paper[142] where a periodic multilayer of alternating ZnS as high-refractive-index material ($n_1 = 2.35$) and MgF_2 as low-refractive-index material ($n_2 = 1.38$) was used. A focus-like effect was observed. The separation between the Ag pinhole and the slab was 150 nm, λ was varied between 120 and 450 nm.

The fabrication of NIMs at optical frequencies encounters basic problems due to difficulties in the selection of the resonator material. Several approaches to solve this problem were suggested,[143] among them: (a) Photonic NIMs composed of split-ring resonators with nanodimensions,[144] (b) nanomaterials consisting of closely packed particles containing an induced magnetic moment and exhibiting high-order multipole resonance,[145] (c) nanoinclusions in resonating plasmonic nanospheres, (d) thin nanocrystalline layers exhibiting surface plasmon resonance. The last approach was realized experimentally[145] using a thin nanocrystalline silver layer. It is important to stress that surface plasmon effects in thin nanocrystalline image-forming (aperture) AgO_x layers (15 nm) were successfully realized already in super-resolution near-field structure (super-RENS) discs. SiC and related materials can be considered as promising materials.[146] SiC has $\varepsilon < 0$ around 10 μm (surface polaritons) and could be used for fabrication of NIM at 1 μm (the cell has to be of the size of 100 nm in this case).

Materials for reversible optical storage recording are also extensively studied.[141] Several materials were suggested, among them (a) GeSbTe phase change alloys exhibiting reversible crystal-amorphous phase transformations, (b) nanocrystalline CdSe films showing tunable reversible photoluminescence, (c) nanocrystalline FePtAg alloys exhibiting transitions fcc $\rightarrow$ tetragonal (magnetic recording), (d) BeFeO, showing melting and crystallization without large deformation. Incidentally, there are several equally important requirements for the material of the recording layer, including: (a) solid state transitions have to be reversible, (b) functionality of all three regimes: Recording (900–1000 K), erasing (700–800 K), readout (low-power laser beam), (c) recorded marks have to be stable, but readily and quickly erasable, (d) Single-phase character of the material.

6. CONCLUSION AND OUTLOOK

We have outlined the most important theoretical, historical, and experimental aspects of negative index materials (NIMs), including a proper mathematical description of fundamental physical laws and equations that may be applied when NIMs are present. In addition to different types of structures that provide NIM properties we also considered structures of photonic crystals that are not pure NIMs but exhibit negative refraction and similar phenomena that are also observed in NIMs. Theoretical studies are currently often complemented by numerical simulations for the detailed analysis of structures with complicated geometry. The corresponding numerical methods were compared and applied to various problems, with a special focus on the NIM slab configuration that promises to overcome the diffraction limit and therefore is the most prominent NIM application. The Maxwell solvers used for the numerical NIM analysis also play an important role for the design of the structures that establish a NIM, for example, wires and split ring resonators that were used in the first NIMs. Linked with appropriate numerical optimizers, such Maxwell solvers are essential for the design of improved NIM structures. Since the currently available NIMs are still far away from desired NIMs for practical use and because promising NIM structures may be highly complex, computer-aided NIM design will play an important role for the progress. Although commercial packages may be applied, there is still a need for more efficient and reliable software.

Currently, the NIM fabrication is much more demanding than the NIM design and optimization, namely at optical frequencies. We have outlined the techniques and structures that are currently most promising. Despite of the fast progress of nanotechnology, we are still at the very beginning of NIM manufacturing. Therefore, we can expect that much better NIMs will become available in the future. This is of high practical importance although Veselago's initial idea already found experimental confirmation by the fabrication and characterization of metamaterials with both negative permittivity and negative permeability. First of all, these experiments were carried out at microwave frequencies where the metamaterial structures may be much larger. Secondly, these metamaterials exhibit NIM properties only for a narrow frequency band and third, these metamaterials are very lossy. Therefore, it is important to reduce the size of the structures, push the frequency range towards optical frequencies, widen the frequency band and reduce the losses.[147] Finally, it will be important to drastically reduce the fabrication costs.

The range of available materials with desired electromagnetic properties may be widened by the design of new artificial structures, i.e., metamaterials composed of different natural materials (dielectrics, metals, semiconductors, etc.) with different shape. This significantly improves the chance of finding high quality NIMs. At the same time it requires strong activities in material research with a focus on electromagnetic properties of composite materials.

Although NIM slabs with a size bigger compared with the wavelength cannot be considered as optical superlenses, thin NIM slabs could open up new opportunities for overcoming the diffraction limit—which could lead to high density optical data storage. Beside this, we expect that the NIM research will intensify the research on more general metamaterials which could lead to new promising materials with new properties and practical applications such as ultra small optical devices that might be important for optical computing.

References

1. D. R. Smith, W. J. Padilla, D. C. Vier, S. C. Nemat-Nasser, and S. Schultz, *Phys. Rev. Lett.* 84, 4184 (**2000**).
2. V. G. Veselago, *Sov. Phys. Usp.* 10, 509 (**1968**).
3. D. V. Sivukhin, *Opt. Spectrosk.* 3, 308 (**1957**), (in Russian).
4. V. E. Pafomov, *Zh. Eksp. Teor. Fiz.* 36, 1853 (**1959**), (in Russian).
5. http://www.wave-scattering.com/negative.html.
6. A. Schuster, *An Introduction to the Theory of Optics*, Edward Arnold, London (**1904**).
7. L. I. Mandelstam, *Zh. Eksp. Teor. Fiz.* 15, 475 (**1945**), (in Russian).
8. V. G. Veselago, *Fiz. Tverdogo Tela* 8, 3571 (**1966**), (in Russian).
9. R. A. Shelby, D. R. Smith, and S. Schultz, *Science* 292, 77 (**2001**).
10. R. B. Gregor, C. G. Parazzoli, K. Li, B. E. C. Koltenbah, and M. Tanielian, *Optic Express* 11, 688 (**2003**).
11. R. Marques, F. Mesa, J. Martel, and F. Median, *IEEE Trans. Antennas Propagat.* 51, 10, 2572 (**2003**).
12. R. W. Ziolkowski, *IEEE Trans. Antennas Propagat.* 51, 1516 (**2003**).
13. G. D. Malyuzhinets, *Zh. Tekh. Fiz.* 21, 940 (**1951**), (in Russian).
14. G. V. Elefteriades and K. G. Balmain, *Negative Refraction Metamaterials*, Wiley-Interscience (**2005**).
15. C. Caloz and T. Ito, *Electromagnetic Metamaterials: Transmission Line Theory and Microwave Applications*, Wiley-Interscience (**2005**).
16. H. Lamb, *Proc. London Math. Soc.* 1, 473 (**1904**).
17. H. C. Poklington, *Nature* 71, 607 (**1905**).
18. Zhen Ye, arXiv:cond-mat/0408477.
19. Y. Zhang, B. Fluegel, and A. Mascaenhas, *Phys. Rev. Lett.* 91, 157404 (**2003**).
20. A. V. Vashkovski and E. G. Lock, *Sov. Phys. Uspekhi* 174, 657 (**2004**), (in Russian).
21. J. B. Pendry, A. J. Holden, D. J. Roberts, and W. J. Stewart, *J. Phys. Condens. Matter* 10, 4785 (**1998**).
22. J. B. Pendry, A. J. Holden, D. J. Roberts, and W. J. Stewart, *IEEE Trans. Micr. Theory. Tech.* 47, 2075 (**1999**).
23. L. P. Gorkov and G. M. Eliashberg, *Sov. Phys. JETP* 21, 942 (**1965**).
24. V. G. Veselago, *Sov. Phys. JETP* 25, 680 (**1967**), (in Russian).
25. P. M. Valanju, R. M. Walser, and A. P. Valanju, *Phys. Rev. Lett.* 88, 187401 (**2002**).
26. J. B. Pendry and D. R. Smith, arXiv:cond-mat/0206563.
27. J. B. Pendry, *Phys. Rev. Lett.* 85, 3966 (**2000**).
28. X. S. Rao and C. K. Ong, cond-mat/0304474.
29. E. Yablonovich, *Phys. Rev. Lett.* 58, 2059 (**1987**).
30. O. Painter, K. Srinivasaan, and P. Barclay, *Phys. Rev. B* 68, 035214 (**2003**).
31. K. Busch, S. Mingaleev, A. Garcia-Martin, M. Schillinger, and D. Hermann, *J. Phys.: Condens. Matter* 15, R1233 (**2003**).
32. E. Istrate, M. Charbonneau-Lefort, and E. Sargent, *Phys. Rev. B* 66, 075121 (**2002**).
33. M. Charbonneau-Lefort, E. Israte, M. Allard, J. Poon, and E. Sargent, *Phys. Rev. B* 65, 125318 (**2002**).
34. J. Albert, C. Jouanin, D. Cassagne, and D. Bertho, *Phys. Rev. B* 61, 4381 (**2000**).
35. L. Braginsky and V. Shklover, *Phys. Rev. B* (accepted).
36. V. Shklover and L. Braginsky, in *Technologies for Optical Countermeasures II; Femtosecond Phenomena and Passive Millimetre-Wave and Terahertz Imaging II*, edited by D. H. Titterton, S. M. Kirkpatrick, R. Stoian, R. Appleby, J. M. Chamberlain, and K. A. Krapels, *Proc. SPIE*, Bellingham (**2005**), Vol. 5989, p. 298.
37. B. Gralak, S. Enoch, and G. Tayeb, *J. Opt. Soc. Am. A* 17, 1012 (**2000**).
38. S. Foteipoulou and C. M. Soukoulis, *Phys. Rev. B* 67, 235107 (**2003**).
39. C. Luo, S. G. Johnson, and J. D. Joannopoulos, *Appl. Phys. Lett.* 81, 2352 (**2002**).
40. A. L. Efros and A. L. Pokrovsky, *Sol. St. Comm.* 129, 643 (**2004**); A. L. Pokrovsky and A. L. Efros, *Sol. St. Comm.* 124, 283 (**2002**).
41. M. Natomi, *Phys. Rev. B* 62, 10969 (**2000**).
42. L. D. Landau and E. M. Lifshitz, *Electrodynamics of Continuous Media*, Pergamon, New York (**1975**).
43. V. G. Veselago, *Physics-Uspekhi* 46, 764 (**2003**).
44. R. A. Shelby, D. R. Smith, S. C. Nemat-Nasser, and S. Schultz, *Appl. Phys. Lett.* 78, 489 (**2001**).
45. J. Witzens, M. Loncar, and A. Scherer, *IEEE J. Sel. Top. Quant. Electr.* 8, 1246 (**2002**).
46. Z.-Y. Li and L.-L. Lin, *Phys. Rev. B* 68, 245110 (**2003**).
47. X. Hu and C. Chan, *Appl. Phys. Lett.* 85, 1520 (**2004**).
48. D. Chigrin, *Phys. Rev. E* 70, 056611 (**2004**).
49. R. Iliew, C. Etrich, and F. Lederer, *Optic Express* 13, 7076 (**2005**).
50. N. Engheta, A. Salandrino, and A. Alu, *Phys. Rev. Lett.* 95, 095504 (**2005**).
51. K. S. Yee, *IEEE Trans. Antennas Propagat.* 14, 302 (**1966**).
52. http://www.remcom.com/xfdtd6/ (**2005**).
53. http://www.optiwave.com/2005/products/optifdtd/index.htm (**2005**).
54. http://www.rsoftdesign.com/products/component_design/FullWAVE/ (**2005**).
55. http://www.empire.de/ (**2005**).
56. T. Weiland, *Electronics and Communications AEUE* 31, 116 (**1977**).
57. http://www.cst.com/Content/Products/MAFIA/Overview.aspx (**2005**).
58. http://www.cst.com/Content/Products/MWS/Overview.aspx (**2005**).
59. J. R. Whiteman, *The Mathematics of Finite Elements and Applications*, John Wiley and Sons, Chichester (**1998**).
60. http://www.ansoft.com/products/hf/hfss/ (**2005**).
61. http://www.ansoft.com/products/em/max3d/ (**2005**).
62. http://www.comsol.com/ (**2005**).
63. H. K. Versteeg and W. Malalasekera, *An Introduction to Computational Fluid Dynamics: The Finite Volume Method*, Addison-Wesley, Reading, MA (**1995**).
64. M. Krumpholz and P. Russer, *IEEE Trans. Microwave Theory Tech.* 42, 1660 (**1994**).
65. http://www.faustcorp.com/ (**2005**).
66. R. F. Harrington, *Field Computation by Moment Methods*, Macmillan, New York (**1968**).
67. D. B. Davidson, Computational Electromagnetics for FR and Microwave Engineering, Cambridge University Press, Cambridge (**2005**).
68. Ch. Hafner, *J. Comput. Theor. Nanosci.* 2, 88 (**2005**).
69. http://www.nec2.org/ (**2005**).
70. http://www.emsci.com/ (**2005**).
71. http://www.feko.info/ (**2005**).
72. http://www.emcos.com/ (**2005**).
73. http://www.boundary-element-method.com/ (**2005**).
74. Ch. Hafner, *The Generalized Multipole Technique for Computational Electromagnetics*, Artech House, Boston (**1990**).
75. A. Taflove, *Computational Electrodynamics*, Artech House, Boston (**1995**).
76. A. Taflove, *Advances in Computational Electrodynamics*, Artech House, Boston (**1998**).
77. A. Taflove and S. Hagness, *Computational Electrodynamics*, 3rd edn., Artech House, Boston (**2000**).
78. K. S. Kunz and R. J. Luebbers, The Finite Difference Time Domain Method for Electromagnetics, CRC Press (**1993**).
79. J.-P. Berenger, *J. Comput. Phys.* 114, 185 (**1994**).
80. Ch. Hafner, *Post-modern Electromagnetics*, John Wiley and Sons, Chichester (**1999**).

REVIEW

81. N. Guérin, S. Enoch, and G. Tayeb, *J. Electromagn. Waves Appl.* 15, 205 (**2001**).
82. http://alphard.ethz.ch/hafner/mmp/mmp.htm (**2000**).
83. F. Bogdanov and D. Karkashadze, *Proc. 3rd Workshop on Electromagnetic and Light Scattering*, Bremen (**1998**).
84. G. Tayeb, R. Petit, and M. Cadilhac, *SPIE* 1545, 95 (**1991**).
85. Y. A. Eremin, N. V. Orlov, and A. G. Shveshnikov, *Comput. Math. Phys.* 35, 731 (**1995**).
86. A. Ludwig, *IEEE AP-S Magazine* 31, 40 (**1989**).
87. P. C. Waterman and R. Truell, *J. Math. Phys.* 2, 512 (**1961**).
88. http://alphard.ethz.ch/hafner/MaX/max1.htm (**2002**).
89. http://www.wiley.co.uk/max-1/ (**2002**).
90. J. C. Slater, *Phys. Rev.* 51, 846 (**1937**).
91. H. van der Lem and A. Moroz, *J. Opt. A: Pure Appl. Opt.* 2, 395 (**2000**).
92. K. H. Johnson, *Phys. Rev.* 150, 429 (**1966**).
93. L. G. Zheng and W. X. Zhang, *Progress in Electromagnetics Research* (*PIER*) 42, 233 (**2003**).
94. http://ab-initio.mit.edu/mpb/ (**2005**).
95. P. Kolinko and D. R. Smith, *Optic Express* 11, 640 (**2003**).
96. J. L. Garcia-Pomar and M. Nieto-Vesperinas, *Optic Express* 12, 2081 (**2004**).
97. X. S. Rao and C. K. Ong, *Phys. Rev. E* 68, 067601 (**2003**).
98. P. F. Loschialpo and D. L. Smith et al., *Phys. Rev. E* 67, 025602 (**2003**).
99. P. F. Loschialpo and D. L. Smith et al., *Phys. Rev. E* 68, 036605 (**2004**).
100. R. W. Ziolkowski, *Opt. Express* 11, 662 (**2003**).
101. J. S. Lih et al., *Europhys. Lett.* 69, 544 (**2005**).
102. J. L. Garcia-Pomar and M. Nieto-Vesperinas, *New J. Physics* 7, 160 (**2005**).
103. Ch. Hafner, J. Smajic, and D. Erni, in *Handbook of Theoretical and Computational Nanosciece*, edited by M. Rieth and W. Schommers, American Scientific Publishers (**2005**).
104. A. Grbic and G. V. Eleftheriades, *Phys. Rev. Lett.* 92, 117403 (**2004**).
105. A. Grbic and G. V. Eleftheriades, *J. Appl. Phys.* 92, 5930 (**2002**).
106. P. P. M. So, H. Du, and W. J. R. Hoefer, *IEEE Trans. Microwave Theory Tech.* 47, 2075 (**2005**).
107. http://www.mathworks.com/ (**2005**).
108. P. Kolinko and D. R. Smith, *Opt. Express* 11, 640 (**2003**).
109. D. O. S. Melville, R. J. Blaikie, and C. R. Wolf, *Appl. Phys. Lett.* 84, 4403 (**2004**).
110. N. Fang, H. Lee, C. Sun, and X. Zhang, *Science* 308, 534 (**2005**).
111. F. J. Rachford, D. L. Smith, P. F. Loschialpo, and D. W. Forester, *Phys. Rev. E* 66, 036613 (**2002**).
112. N.-C. Panoiu and R. M. Osgood, Jr., *Phys. Rev. E* 68, 016611 (**2003**).
113. C. Luo, S. G. Johnson, and J. D. Joannopoulos, *Phys. Rev. B* 65, 201104 (**2002**).
114. C. Luo, S. G. Johnson, and J. D. Joannopoulos, *Appl. Phys. Lett.* 81, 2352 (**2002**).
115. X. Wang, Z. F. Ren, and K. Kempa, *Optic Express* 12, 2919 (**2004**).
116. K. Yasumoto (ed.), Electromagnetic Theory and Applications for Photonic Crystals, CRC Press, Boca Raton, FL (**2006**).
117. S. Linden, C. Enkrich, M. Wegener, J. Zhou, T. Koschny, and C. M. Soukoulis, *Science* 306, 1351 (**2004**).
118. C. Caloz and T. Itoh, *IEEE Trans. Antennas Propagat.* 52, 1159 (**2004**).
119. A. K. Iyer, P. C. Kremer, and G. V. Eleftheriades, *Opt. Express* 11, 696 (**2003**).
120. K. Aydin, K. Guven, M. Kafesaki, L. Zhang, C. M. Soukoulis, and E. Ozbay, *Opt. Lett.* 29, 2623 (**2004**).
121. T. J. Yen, W. J. Padilla, N. Fang, D. C. Vier, D. R. Smith, J. B. Pendry, D. N. Basov, and X. Zhang, *Science* 303, 194 (**2004**).
122. S. O'Brien and J. B. Pendry, *J. Phys. Condens. Matter* 14, 6383 (**2002**).
123. S. Zhang, W. Fan, B. K. Minhas, A. Frauenglass, K. J. Malloy, and S. R. J. Brueck, *Phys. Rev. Lett.* 94, 03702 (**2005**).
124. A. N. Grigorenko, A. K. Geim, H. F. Gleeson, Y. Zhang, and I. Y. Khrushchev, *J. Petrovic. Nature* 438, 335 (**2005**).
125. P. V. Parimi, W. T. Lu, P. Vodo, J. Sokoloff, J. S. Derov, and S. Sridhar, *Phys. Rev. Lett.* 92, 127401 (**2004**).
126. E. Cubukcu, K. Aydin, E. Ozbay, S. Foteinopoulou, and C. M. Soukoulis, *Nature* (*London*) 423, 604 (**2003**).
127. R. Gajic, F. Kuchar, R. Meisels, J. Radovanovic, K. Hingerl, J. Zarbakhsh, J. Stampfl, and A. Woesz, *Z. Metallk* 95, 618 (**2004**).
128. P. Vodo, P. V. Parimi, W. T. Lu, and S. Sridhar, *Appl. Phys. Lett.* 85, 1858 (**2004**).
129. E. Di Gennaro, P. V. Parimi, W. T. Lu, S. Sridhar, J. S. Derov, and B. Turchinetz, *Phys. Rev. B* 72, 033110 (**2005**).
130. A. Berrier, M. Mulot, M. Swillo, M. Qiu, L. Thylen, A. Talneau, and S. Anand, *Phys. Rev. Lett.* 93, 073902 (**2004**).
131. J. B. Pendry, *Science* 306, 1353 (**2004**).
132. C. Caloz and T. Itoh, *Abstr. EPFL Latsis Symposium Negative Refraction: Revisiting Electromagnetics from Microwaves to Optics*, Lausanne (**2005**); C. Calos and T. Itoh, *IEEE Trans. Antennas Propagat.* 52, 1159 (**2004**).
133. A. Lai, T. Itoh, and C. Caloz, *Abstr. EPFL Latsis Symposium Negative Refraction: Revisiting Electromagnetics from Microwaves to Optics*, Lausanne (**2005**); I. Lin, M. DeVicentis, C. Calos, and T. Ito, *IEEE Trans. Microwave Theory Tech.* 52, 1142 (**2004**); I. Lin, C. Calos, and T. Itoh, *IEEE-MTT Int. Symp. Dig.* 1, 325 (**2003**); A. Sanada, C. Calos, and T. Itoh, *IEEE Trans. Microwave Theory Tech.* 52, 4 (**2004**). C. Calos, A. Lai, and T. Itoh, *IEEE AP-S USNC/URSI National Radio Science Meeting*, Monterey, CA (**2004**). A. Lai, T. Itoh, and C. Calos, *IEEE AAP-SUSNC/URSI National Radio Science Meeting*, Washington, DC (**2005**).
134. M. Galli, D. Bajoni, F. Marabelli, L. C. Andreani, L. Pavesi, and G. Pucker, *Phys. Rev. B* 69 115107 (**2004**).
135. K. Inoue, N. Kawai, Y. Sugimoto, N. Carlsson, N. Ikeda, K. Asakawa, *Phys. Rev. B* 65, 121308 (**2002**).
136. V. G. Veselago, *Abstr. EPFL Latsis Symposium Negative Refraction: Revisiting Electromagnetics from Microwaves to Optics*, Lausanne (**2005**).
137. C. G. Parazzoli, R. B. Greegor, J. A. Nielsen, M. A. Thompson, K. Li, A. M. Vetter, M. H. Tanielian, and D. C. Vier, *Appl. Phys. Lett.* 84, 3232 (**2003**).
138. P. Vodo, P. V. Parimi, W. T. Lu, and S. Sridhar, *Appl. Phys. Lett.* 86, 201108 (**2005**).
139. C. G. Parazzoli, R. B. Greegor, B. E. C. Koltenbah, J. A. Nielsen, M. A. Thompson, and M. H. Tanielian, *Abstr. EPFL Latsis Symposium Negative Refraction: Revisiting Electromagnetics from Microwaves to Optics*, Lausanne (**2005**).
140. Metamorphose. Network of Excellence, http://www.metamorphose-eu.org
141. M. Laurencis, M. Förster, P. H. Bolivar, and H. Kurz, *Jap. J. Appl. Phys. B* 43, 4700 (**2004**).
142. T. Fukaya and J. Tominaga, *J. Opt. Soc. Am. B* 21, 1280 (**2004**).
143. N. Engheta, *Abstr. EPFL Latsis Symposium Negative Refraction: Revisiting Electromagnetics from Microwaves to Optics*, Lausanne (**2005**).
144. S. O'Brien, D. McPeake, S. A. Ramakrishna, and J. B. Pendry, *Phys. Rev. B* 69, 241101 (**2004**).
145. G. Shvets and Y. A. Urzhumov, *Phys. Rev. Lett.* 93, 243902 (**2004**).
146. C. Rockstuhl, M. G. Salt, and H. P. Herzig, *J. Opt. Soc. Amer. B* 22, 481 (**2005**).
147. A. A. Houck, J. B. Brock, and I. L. Chuang, *Phys. Rev. Lett.* 90, 137401 (**2003**).

Received: 4 January 2006. Accepted: 11 January 2006.